Title

A Legionella toxin exhibits tRNA mimicry and glycosyl transferase activity to target the translation machinery and trigger a ribotoxic stress response

Journal

Nature Cell Biology, 25(11)

ISSN

1465-7392

Authors

Subramanian, Advait
Wang, Lan
Moss, Tom
et al.

Publication Date

2023-11-01

DOI

10.1038/s41556-023-01248-z

Peer reviewed

HHS Public Access

Author manuscript

Nat Cell Biol. Author manuscript; available in PMC 2024 November 01.

Published in final edited form as:

Nat Cell Biol. 2023 November ; 25(11): 1600–1615. doi:10.1038/s41556-023-01248-z.

A *Legionella* toxin exhibits tRNA mimicry and glycosyl transferase activity to target the translation machinery and trigger a ribotoxic stress response

Advait Subramanian[1,2,3,*], **Lan Wang**[3,*], **Tom Moss**[1,2], **Mark Voorhies**[2], **Smriti Sangwan**[3], **Erica Stevenson**[4,5,6], **Ernst H. Pulido**[4], **Samentha Kwok**[7], **Robert J. Chalkley**[8], **Kathy H. Li**[8], **Nevan J. Krogan**[4,5,6], **Danielle L. Swaney**[4,5,6], **Alma L. Burlingame**[8], **Stephen N. Floor**[7,9], **Anita Sil**[2,10], **Peter Walter**[3,11,#,$], **Shaeri Mukherjee**[1,2,10,#]

[1]G.W. Hooper foundation, University of California at San Francisco, San Francisco, USA.

[2]Department of Microbiology and Immunology, University of California at San Francisco, San Francisco, USA.

[3]Department of Biochemistry and Biophysics, University of California at San Francisco, San Francisco, USA.

[4]Gladstone Institute of Data Science and Biotechnology, J. Gladstone Institutes, San Francisco, USA.

[5]Department of Cellular and Molecular Pharmacology, University of California at San Francisco, San Francisco, USA.

[6]Quantitative Biosciences Institute, University of California at San Francisco, San Francisco, USA.

[#]Corresponding authors: shaeri.mukherjee@ucsf.edu; pwalter@altoslabs.com.

[*]Authors contributed equally

[$]current address: Bay Area Institute of Science, Altos Labs, Redwood City, USA.

Author Contributions Statement

Conceptualization, A.Su., S.M.; Methodology, A.Su., L.W., T.M., M.V., S.S., D.L.S., R.J.C., N.J.K., S.F., A.Si., P.W., S.M.; Investigation, A.Su., L.W., T.M., M.V., E.S., E.H.P., S.K., D.L.S., R.C., K.L.; Formal Analysis, A.Su., L.W., M.V., D.L.S., R.J.C.; Writing – Original Draft, A.Su., L.W., S.M.; Writing – Review & Editing, A.Su., L.W., M.V., A.Si., P.W., S.M.; Visualization, A.Su., L.W., S.M.; Funding Acquisition, P.W., S.M.; Resources, S.S., A.L.B., S.F.; Supervision, A.Su., D.L.S., N.J.K., A.Si., P.W., S.M..

Competing Interests Statement

P.W. is an inventor on U.S. Patent 9708247 held by the Regents of the University of California that describes ISRIB and its analogues. Rights to the invention have been licensed by UCSF to Calico. The N. J. K. laboratory has received research support from Vir Biotechnology, F. Hoffmann-La Roche, and Rezo Therapeutics. N. J. K. has financially compensated consulting agreements with the Icahn School of Medicine at Mount Sinai, New York, Maze Therapeutics, Interline Therapeutics, Rezo Therapeutics, GEn1E Lifesciences, Inc, and Twist Bioscience Corp. He is on the Board of Directors of Rezo Therapeutics and is a shareholder in Tenaya Therapeutics, Maze Therapeutics, Rezo Therapeutics, and Interline Therapeutics. D. L. S. has a consulting agreement with Maze Therapeutics and Rezo Therapeutics. All other authors declare no competing interests.

Code Availability Statement

MaxQuant and Protein Prospector (v6.3.23) software required for analysis of raw MS data are available at https://www.maxquant.org/ and https://prospector.ucsf.edu/prospector/mshome.htm respectively. For Cryo-EM image processing and data analysis, the micrograph frames were aligned using MotionCor2[73] (RRID: SCR_016499). The contrast transfer function (CTF) parameters were estimated with GCTF[74] (RRID: SCR_016500). Particles were picked using Gautomatch (developed by Kai Zhang, https://www2.mrc-lmb.cam.ac.uk/research/locally-developed-software/zhang-software/#gauto) without a template. Particles were extracted using a 64-pixel box size and classified in 2D in Relion[75] (RRID: SCR_016274). Particles were imported to cryoSPARC[76] (RRID: SCR_016501) for homogeneous refinement and heterogeneous refinement. Structure prediction analysis was performed using RaptorX[77] (RRID: SCR_018118). Models were manually adjusted in Coot[79] (RRID: SCR_014222). Model refinement was performed in Phenix[80] (RRID: SCR_014224) Molecular graphics and analyses were performed with the UCSF Chimera package[82] (RRID: SCR_004097). ICE CRISPR Analysis tool from Synthego was used to analyze KO efficiency of cell lines and is available at https://www.synthego.com/products/bioinformatics/crispr-analysis.

[7]Department of Cell and Tissue Biology, University of California at San Francisco, San Francisco, USA.

[8]Mass Spectrometry Facility, Department of Pharmaceutical Chemistry, University of California at San Francisco, San Francisco, USA.

[9]Helen Diller Family Comprehensive Cancer Center, University of California, San Francisco, San Francisco, USA.

[10]Chan Zuckerberg Biohub, San Francisco, USA.

[11]Howard Hughes Medical Institute.

Abstract

A widespread strategy employed by pathogens to establish infection is to inhibit host cell protein synthesis. *Legionella pneumophila*, an intracellular bacterial pathogen and the causative organism of Legionnaires' disease, secretes a subset of protein effectors into host cells that inhibit translation elongation. Mechanistic insights into how the bacterium targets translation elongation remain poorly defined. We report here that the *Legionella* effector SidI functions in an unprecedented way as a transfer RNA (tRNA) mimic that directly binds to and glycosylates the ribosome. The 3.1 Å cryo-EM structure of SidI reveals an N-terminal domain with an 'inverted-L' shape and surface charge distribution characteristic of tRNA mimicry and a C-terminal domain that adopts a glycosyl transferase fold that licenses SidI to utilize GDP-mannose as a sugar precursor. This coupling of tRNA mimicry and enzymatic action endows SidI with the ability to block protein synthesis with a potency comparable to ricin, one of the most powerful toxins known. In *Legionella* infected cells, the translational pausing activated by SidI elicits a stress response signature mimicking the ribotoxic stress response, which is activated by elongation inhibitors that induce ribosome collisions. SidI-mediated effects on the ribosome activate the stress kinases ZAKα and p38, which in turn drive an accumulation of the protein activating transcription factor 3 (ATF3). Intriguingly, ATF3 escapes the translation block imposed by SidI, translocates to the nucleus, and orchestrates the transcription of stress-inducible genes that promote cell death, revealing a major role for ATF3 in the response to collided ribosome stress. Taken together, our findings elucidate a novel mechanism by which a pathogenic bacterium employs tRNA mimicry to hijack a ribosome-to-nuclear signaling pathway that regulates cell fate.

Legionella pneumophila (*L.p.*) is an intracellular bacterial pathogen that secretes ~300 protein effectors via its type IV secretion system (T4SS) into an infected cell. A vital process targeted by a subset of translocated *L.p.* effectors is protein synthesis[1–6]. Seven of these effectors contribute to a slowing down of translation elongation rates[5–7,1,3] and cause an accumulation of stalled ribosomes in *L.p.* infected cells as measured by an increased ribosome occupancy along the length of messenger RNAs (mRNAs) in ribosome run-off assays[1].

Amongst the secreted elongation inhibitors (EITs), the *Legionella* glucosyl transferase family of proteins (Lgt 1–3) glycosylate the eukaryotic elongation factor eEF1A using UDP-glucose as a sugar precursor[2,7], while the *Legionella* kinase LegK4 phosphorylates the ribosome-associated chaperone HSC70[6]. The EIT SidI (substrate of icm/dot transporter-I)

has been proposed to bind directly to eEF1A and to another elongation factor, eEF1Bγ[5] and to function as a glycosyl-hydrolase that cleaves GDP-linked sugar precursors[8]. Nevertheless, a mechanistic understanding of how SidI reduces translation elongation rates is lacking.

The *L.p.* EITs elicit at least two common cellular outcomes and hence are presumed to have redundant roles. First, the heterologous expression of individual EITs in yeast and mammalian cells results in cell death[2,3,5–7,9]; and, second, the secretion of five EITs, namely Lgt 1–3, SidI, and SidL, is essential for the robust activation of the mitogen activated protein kinases (MAPKs) p38 and JNK in infected cells[10].

Recent evidence indicates that in certain instances of translation stress, ribosome stalling events may lead to collisions between the stalled ribosome and the trailing ribosome on the mRNAs being translated[11]. In response to a build-up of such aberrant translation intermediates, cells have been shown to trigger multiple ribosome-associated signaling networks[12,13]. These include the integrated stress response (ISR)[14] and the ribotoxic stress response (RSR)[15]. It has been suggested that consequent to the increase in the amount of colliding ribosomes in cells, the activation of the ISR promotes cell survival, while the RSR, paradoxically, promotes cell death[12]. The ISR is a signaling pathway that is turned on by the phosphorylation of serine 51 (S51) on the alpha subunit of the translation initiation factor eIF2[14]. The RSR, instead, is characterized by the activation of p38 and JNK MAPKs[12,15,16]. Both signaling networks are governed by the recruitment of the leucine-zipper and sterile α motif kinase ZAKα (MAP3K20) to collided ribosomes and its subsequent activation by auto-phosphorylation[12,16]. Whether infection with pathogenic *Legionella* provokes such responses from host cells remains to be determined.

In this study, we reconcile these seemingly disparate observations by providing mechanistic insights into the function of the *Legionella* EIT SidI. Through a combination of biochemical, structural, and genetic experiments, we show that SidI is a highly potent tRNA mimic that fundamentally rewires host cell physiology to activate a ribotoxic stress response pathway.

SidI potently inhibits protein synthesis and binds to ribosomes

As a test of their redundancy, we first set to address if N-terminally GST-tagged versions of Lgt2, SidI, SidL, LegK4 Δ1–58 (labelled as LegK4) and RavX (Figure 1a) are equipotent in their capacity to inhibit the translation of a reporter luciferase mRNA in cell free translation extracts. The incubation of GST-SidI with the translation extract elicited strong inhibition of protein synthesis (Figure 1b) with a measured half-maximal inhibitory concentration (IC_{50}) of ~900 picomolar, which is ~100-fold to ~1000-fold more potent than the other tested *L.p.* EITs (Figure 1c) and comparable to the potency of the toxin ricin (~150 picomolar)[17]. In line with these results, the transient expression of SidI fused to a N-terminal FLAG-tag (FLAG-SidI) in HEK293T cells also induced a strong inhibition (~90%) of protein synthesis rates as measured by puromycin pulse/chase assays (Extended Data Figure 1a–b).

To determine the putative target(s) of SidI in mammalian cells, we undertook an unbiased proteomics approach to identify the interacting partners in cell extracts by affinity purification coupled to mass spectrometry (AP-MS). Our analyses revealed a conserved

set of 81 interacting partners that were either uniquely detected or enriched after GST-SidI pulldowns in at least two out of the three AP-MS experiments (Extended Data Figure 1c, Supplementary Table 1). Forty-five percent of these interactors (37/81) were *bona fide* components of the cellular protein synthesis apparatus and included multiple ribosomal proteins, elongation factors and tRNA ligases (Figure 1d, Extended Data Figure 1d).

Because of the enrichment of both large and small ribosomal subunit proteins in our SidI pulldown eluates (Extended Data Figure 1d), we asked if SidI might bind to ribosomes. Indeed, SidI directly interacted with individual ribosomes (80S ribosome fraction) purified from cell extracts (Figure 1e). SidI also precipitated elongation factor EEF1A and a repertoire of tRNA ligases from HEK293T cell extracts (Figure 1f). Importantly, SidI and ribosomes robustly co-sedimented in the 80S and polysome fractions after *in vitro* translation reactions (Figure 1g, fractions 4 – 8), indicating that SidI engages with actively translating ribosomes in these cell free extracts.

These initial findings focused our efforts to understand the mechanism of action of SidI.

Structural analyses of SidI by cryo-EM reveals molecular mimicry

To gain further mechanistic insights, we next determined the structure of full-length SidI (110kD) with an N-terminal GST tag using single particle cryo-electron microscopy (cryo-EM). A consensus structure (from 749,000 particles) yielded a map with an average resolution of 3.1 Å, approaching 2.5 Å in the core, with most side chain density well-resolved (Figure 2a, Extended Data Figure 2, Supplementary Table 2; PDB ID: 8JHU). We observed no density representing the GST-tag, as it was likely averaged out during reconstruction due to a flexible linkage between GST and SidI.

SidI adopts a glycosyl transferase B fold

The 3D model of SidI shows that the C-terminal domain possesses two subdomains (B and C) with Rossman-like folds that are connected by a flexible hinge region (Figure 2b, o; blue and yellow), with a putative nucleotide-sugar binding pocket located within a cleft between the two subdomains (Figure 2b; arrow). Domains containing Rossman-like folds are often found in enzymes and are composed of a series of alternating β-strands and α-helices that confer a three-layered sandwich structure that binds nucleotide cofactors. This domain architecture is highly conserved in a group of glycosyl transferases (GTs) that adopt the GT-B fold[18].

We compared the structure of domains B and C to that of a known mannosyl transferase, the *C. glutamicum* enzyme PimB' (PDB ID: 3OKA)[19]. An overlay of PimB' (Figure 2c) to SidI showed a close match between their secondary structures (Figure 2d), with a conservation of amino acids that form the catalytic pocket in both proteins (Figure 2e, Extended Data Figure 3d). In particular, the first fifty amino acids of domain A folds on top of domains B and C and together they constitute the GT domain of SidI (Figure 2b). In agreement with our data and previous work[8], we determined that SidI hydrolyzed GDP from GDP-mannose most efficiently, while the hydrolysis of GDP from GDP-fucose was less efficient (Extended Data Figure 3b–c). The hydrolysis of UDP from UDP-glucose by SidI was undetectable under

our assay conditions. By contrast, Lgt2, an *L.p.* EIT that adopts the GT-A fold[2,8,20] only catalyzed the release of UDP from UDP-glucose (Extended Data Figure 3a).

On examining the GDP-mannose binding pocket of SidI, we focused our attention on the amino acids K600, D724 and R453 (Figure 2e). K600 and D724 are conserved in PimB' (Extended Data Figure 3d) and single point mutations in the analogous residues K211Q and E290N on PimB' result in significant defects in GDP-mannose binding efficiency and enzymatic function, suggesting that these residues help in accommodating GDP-mannose within the enzymatic pocket[19]. R453 does not appear to contact GDP-mannose directly. However, it is involved in a network of interactions across domains A and B, primarily ionic interactions with D19, D456 and E482, as well as a cation-π interaction with F11 (Figure 2e). These interactions may stabilize the local conformation, thus enabling the enzymatic pocket to be correctly positioned for catalysis. Indeed, previous studies have shown that a R453P mutation significantly attenuates SidI function[5,8].

SidI possesses a tRNA-mimicry domain

An important feature of SidI's domain architecture lies in three characteristic distinct kinks in its overall structure. One kink of near 90 degrees is located in the GT domain (Extended Data Figure 3e; panel 1). Another kink of ~60 degrees lies in domain A that connects this domain to a helical bundle (Extended Data Figure 3e; panel 3). A third kink revealed a noticeable 90-degree angle that connects domains A and B. Together, this domain architecture confers a striking 'inverted L-shape' (Figure 2f, Extended Data Figure 3e; panel 2), characteristic of the shape of a tRNA molecule. An overlay of the structure of SidI's domains A and B (excluding the 50 amino acids that form the enzymatic cleft) to the structure of a tRNA showed a tight fit into the space occupied (Figure 2h), with both showing a near 90-degree angle between the two arms. This region of SidI is around 67 Å long and 65 Å wide, similar in both size and width of tRNAs which are 70 Å long and 60 Å wide (Figure 2f–h), and architecturally similar to domains on proteins that are known to function as tRNA mimics in cells, such as the eukaryotic elongation factor EEF2[21], the eukaryotic release factor eRF1[22] and the bacterial elongation factors EF-G[23] and EF-P[24] (Figures 2i–l), although SidI is ~30 Å thicker than the tRNA due to a helical bundle extending from domain A (Figure 2h).

In addition to the resemblance in sizes and shapes, we found a stretch of positively charged amino acids that are conserved between these tRNA mimicking proteins and SidI (Figure 2m–n, Extended Data Figure 3f). This positively charged stretch on SidI comprises of five lysine (K) residues and is present on a short loop region at the edge of domain A that connects two alpha helices (Figure 2m; box). In comparison, such features are also shared by domain IV of EEF2 (Figure 2n; boxes) that facilitate complex interactions with translating ribosomes[21] (Extended Data Figure 4a–c). Molecular docking analyses of SidI onto the structure of the ribosome bound to EEF2[21] suggests how the positively charged loop of SidI might enable it to interact with the ribosome (Extended Data Figure 4a–c). Accordingly, we henceforth refer to the N-terminal domain as SidI's tRNA-mimicry domain (Figure 2o).

tRNA mimicry and enzymatic activity explains SidI potency

To address if and how the above structural features of SidI impact its function, we attempted to decouple the influence of the GT domain from the tRNA mimicry domain by introducing point mutations either in the enzymatic pocket (Figure 2e) or in the positively charged loop region of domain A (Figure 2m).

We expressed and purified GST-SidI bearing R453P, K600Q and D724N mutations in the enzymatic pocket as well as GST-SidI with a mutated K-rich loop in the tRNA mimicry domain (K167A; K169A; K170A; K172A; K174A; SidI K-loop mutant). Introducing these mutations did not perturb the overall fold of SidI as the mutant and wild-type proteins exhibited similar thermal stabilities (Extended Data Figure 3g). Importantly, only mutations to the enzymatic pocket of SidI affected its ability to hydrolyze GDP-mannose, while the K-rich loop mutant showed no defect (Figure 3a). In further support of a successful decoupling of structural tRNA mimicry and enzymatic activity, the GST-SidI K-loop mutant failed to efficiently bind to ribosomes purified from cell extracts and co-sedimented poorly with fractions containing translating ribosomes after *in vitro* translation reactions (Figure 3b–c), whereas the enzymatic-deficient GST-SidI R453P mutant robustly enriched purified ribosomes and co-sedimented with fractions containing translating ribosomes.

Interestingly, pulldowns of both the GST-SidI K-loop mutant and GST-SidI R453P equally precipitated a repertoire of tRNA ligases and EEF1A from HEK293T lysates (Extended Data Figure 5a–b). Remarkably, however, all four mutant proteins were two orders of magnitude less potent at inhibiting luciferase mRNA translation in comparison to SidI (Figures 3d–e). Taken together, these results demonstrate that ribosomes are a major target of SidI action. Furthermore, they also suggest that while the K-rich loop in the tRNA-mimicry domain of SidI confers the specificity to target the ribosome, the glycosyl transferase activity of SidI might provide its potency to inhibit protein synthesis.

To test this hypothesis, we first pre-treated translation extracts with GST-SidI or GST-SidI R453P at 1 nM (~IC_{50} of SidI) for varying durations. In addition, we also pre-treated RRL extracts with GST-SidI R453P at 0.5 μM (~IC_{50} of SidI R453P). We then utilized these pre-treated extracts to translate luciferase mRNA *in vitro* for another 60 minutes. Preincubation of RRL extracts with SidI resulted in a progressive reduction of translation efficiency relative to the increase of SidI pre-treatment time (Figure 3f), consistent with the model that the enzymatic action of SidI is required for its potency. By contrast, preincubation with SidI R453P at the same concentration (1nM) or at an ~1000-fold higher concentration (0.5μM) did not result in a changed translation efficiency at all pre-treatment times tested (Figure 3f), supporting the notion that the R453P mutant was inhibiting protein synthesis at high concentrations because of its tRNA mimicry and not due to residual enzymatic activity. These results also indicate that both the enzymatic function of SidI and its tRNA-like shape are important to potently inhibit protein synthesis.

We reaffirmed these findings by experiments performed in cell-free translation extracts (S30) isolated from *E.coli*. Incubating GST-SidI or GST-SidI R453P with S30 extracts resulted in a modest inhibition of luciferase mRNA translation at micromolar concentrations

(Figure 3g; no GDP-mannose). Supplementing these extracts with GDP-mannose vastly accelerated translation inhibition under reaction conditions where GST-SidI but not GST-SidI R453P was present (Figure 3g; + GDP-mannose), indicative of a conserved mechanism by which SidI inhibits protein synthesis in both bacteria and eukaryotes. We note that supplementing eukaryotic rabbit-reticulocyte-lysate extracts with exogenously added GDP-mannose did not influence the rates of translation inhibition induced by GST-SidI (Figure 3h), likely because GDP-mannose is not limiting in eukaryotic lysates.

SidI glycosylates ribosomes

We next reasoned that ribosomes might serve as enzymatic substrates for SidI mediated translation inhibition. Incubation of increasing concentrations of ribosome extracts with GST-SidI but not GST-SidI R453P resulted in a dose-dependent increase in the rate of GDP hydrolysis from GDP-mannose (Figure 4a), suggesting that SidI catalyzes a rate of GDP hydrolysis that is directly proportional to the transfer of mannose to one or more acceptor substrate(s) present in these extracts. To directly test the transfer of mannose to ribosomes, we added radio-labelled GDP-H^3-mannose (where the mannose moiety is tritiated) as a nucleotide sugar precursor to enzymatic reactions and determined the efficiency of H^3-mannose transfer onto acceptor substrates. In strong support of glycosyl transferase activity, we detected an approximately two-fold greater amount of H^3-mannose labelled GST-SidI in comparison to the GST-SidI R453P mutant (Figure 4b), indicating that SidI itself is auto-mannosylated. Indeed, several *L.p.* effectors with enzymatic domains show evidence of autocatalysis[25–27]. Strikingly, in the pulldown eluates containing GST-SidI and ribosomes, we detected a further eight-fold increase of H^3-mannose labelled molecules as compared to GST-SidI alone (Figure 4b, second and fourth bars). Given that equimolar amounts of GST-SidI and GST-SidI R453P were present in the enzymatic reactions with/without ribosomes, the significant amounts of H^3-mannose labelling detected only in the eluates with GST-SidI and ribosomes firmly indicates that SidI catalyzes the transfer of H^3-mannose from GDP-H^3-mannose onto ribosomes.

We then determined if some of the ribosomal proteins that bound to SidI exhibited affinity to the mannose-binding lectin concanavalin-A coupled to Sepharose beads (Con-A) (Figure 4c, schematic). Con-A pulldowns strongly enriched the ribosomal proteins uL4, uL3 and eS8, only when the ribosome extracts were incubated with GST-SidI and GDP-mannose (Figure 4c; lane 6). Incubation of ribosome extracts containing GDP-mannose with either GST or GST-SidI R453P resulted in little to no enrichment of the proteins by Con-A (Figure 4c; lanes 4 and 8). Interestingly, Con-A also only bound to GST-SidI strongly under conditions where the effector was incubated with GDP-mannose (Figure 4c; lanes 6 and 10), confirming the notion that SidI itself becomes auto-mannosylated.

To further substantiate these results, we sought to determine the repertoire of ribosomal proteins enriched by Con-A pulldowns by mass spectrometry (Extended Data Figure 4d; schematic). In a strong validation of our findings, twenty five ribosomal proteins (including uL3, uL4, eS8) and SidI were selectively enriched by Con-A from reactions where GST-SidI was incubated with the ribosome extracts and GDP-mannose (Supplementary Table 3, Extended Data Figure 4e). By mapping these proteins onto the structure of the ribosome

(PDB ID:6GZ5)[21], we determined that eleven proteins localized at or near the A-site/P-site of the ribosome while four proteins localized to the peptide-exit tunnel, just above the ribosomal P-site (Extended Data Figure 4f–g).

SidI induces ribosome collisions in cells

In line with the *in vitro* data, FLAG-SidI expression resulted in a substantial reduction of nascent protein synthesis rates (Figure 4d) and an increase in the number of sedimented polysomes (Figure 4f), while FLAG-SidI R453P expression did not, indicating an accumulation of stalled ribosomes on mRNAs in SidI expressing cells.

In light of recent evidence suggesting that ribosome stalling leads to ribosome collisions between the stalled and trailing ribosome[12,28], we treated the lysates from HEK293T cells expressing either FLAG-SidI or FLAG-SidI R453P with the non-specific RNase (RNase-A) and resolved these ribosome populations on a sucrose gradient. Analyses of the profiles determined that a majority of the ribosomes collapsed to monosomes under both these conditions (Figure 4f; + RNase A). Noticeably, however, we observed a relative enrichment of RNase-A resistant disomes in cells expressing FLAG-SidI but not in cells expressing FLAG-SidI R453P (Figure 4f; + RNase A). To further corroborate these findings, we monitored the ubiquitylation of the ribosomal protein eS10 that occurs when ribosomes collide[13,28]. Indeed, immunoblotting of lysates from cells expressing FLAG-SidI but not FLAG-SidI R453P resulted in the accumulation of an ~8kD heavier pool of eS10, corresponding to the molecular weight of the mono-ubiquitylated ribosomal protein (Figure 4e). Together, these results indicate that catalytically active SidI, when expressed in cells, induces translation elongation defects that cause ribosome collisions.

SidI activates a ribosome-associated stress response

Perturbations that result in ribosome collisions often activate signaling and transcriptional quality control programs[12,13,16,29]. We reasoned that *L.p.*, by way of secreting SidI, might activate some of these programs in infected cells (Figure 5a). To that end, we first employed RNA sequencing (RNA-seq) to reveal the changes in mRNA abundance in Fc gamma receptor expressing HEK293 (HEK293-FcγR) cells infected either with wild type (WT) *L.p.* or an isogenic T4SS defective mutant of *L.p.* (*ΔdotA L.p.*) that fails to secrete any effectors[30,31] (Figure 5b, Supplementary Table 4). In independent experiments, we induced ribosome collisions in HEK293T cells by treating them with mild doses (0.1 μM) of the elongation inhibitors anisomycin (ANS)[12,13,28] and didemnin-B (DD-B)[28,32] and analyzed their respective transcriptomes by RNA-seq (Figure 5b).

Principal component analysis showed that the transcriptomes of cells treated with ANS or DD-B clustered together, indicating that the response to ribosome collisions elicited a conserved signature (Extended Data Figure 6a). The transcriptomes of WT *L.p.* infected cells, although indicative of a general host response to bacterial infection by gene set enrichment analyses[33] (Supplementary Table 5), differed in a manner dependent on the duration of infection (Extended Data Figure 6a) and varied from the transcriptomes of ANS and DD-B treated cells. Despite the variance in the global transcriptional profiles,

a conserved set of 75 genes was significantly co-regulated in cells infected for 4 hours with WT *L.p.* and in cells treated for 4 hours with either ANS or DD-B (Figure 5c). ~20% of the upregulated transcripts (13/61) mapped to pathways involved in stress signaling and cell death (Figure 5d), and their abundance was dynamically regulated during infection (Extended Data Figure 6b). No specific commonalities could be attributed to the downregulated genes. Assuredly, a study had reported that a subset of these transcripts are also highly abundant in *L.p.* infected bone marrow derived macrophages (BMDMs) from WT and *Myd88* knockout mice[34] (Extended Data Figure 7a). We confirmed these findings with a targeted validation of five highly upregulated transcripts (*ATF3*, *TNFRSF12A*, *HSPB8*, *PPP1R15A*, *GADD45A*) by quantitative real time polymerase chain reaction (qRT-PCR) assays. WT *L.p.* but not *ΔdotA L.p.* infected HEK293-FcγR cells activated a robust increase in the mRNA abundance of all five transcripts that peaked at 8 hours post infection in comparison to uninfected cells (Figure 5e). HEK293T cells treated with mild doses of ANS, DD-B and deoxynivalenol (DON) also strongly activated stress transcript induction, while cycloheximide (CHX) and harringtonine (HTN) treatments resulted in detectably lower inductions of *ATF3*, *TNFRSF12A*, *HSPB8* and *PPP1R15A* (Extended Data Figures 7d–h). We note that ANS, DD-B and DON specifically interfere with an early step of the translation elongation cycle[32,35], suggesting that an inhibition of this particular step renders cells hyper-sensitive to stalled ribosome stress. Moreover, a muted response to CHX or HTN excludes a causal role for general protein synthesis inhibition to activate an upregulation of these specific transcripts. Concordantly, FLAG-SidI expression also activated stress transcript induction in comparison to FLAG-SidI R453P (Extended Data Figures 7d–h), supporting the notion that SidI is necessary and sufficient to induce the stress response.

To confirm if these observations parallel *L.p.* infections, we utilized an isogenic mutant strain of *L.p.* with genomic deletions of five EITs, including *sidI* (*Δlgt1*, *Δlgt2*, *Δlgt3*, *ΔsidI* and *ΔsidL*; hereafter *Δ5*)[3] and a *Δ5* strain complemented with a plasmid encoding *sidI* (*Δ5+sidI*). Cells infected with *Δ5 L.p.* exhibited minimal changes in stress transcript abundance, with mRNA levels similar to those observed during infections with *ΔdotA L.p.* (Figure 5e). Importantly, cells infected with the complemented *Δ5+sidI L.p.* strain induced all five stress inducible transcripts significantly (Figure 5e), albeit not to the quantities observed during infections with WT *L.p.* for all transcripts except *HSPB8* (Figure 5e). These results indicate that, while SidI secretion is sufficient for the stress transcript induction during *L.p.* infection, other possible T4SS effectors also regulate their abundance.

Interestingly, *ATF3* mRNA was the most differentially expressed transcript co-upregulated under all treatment conditions (Figure 5d–e). Its protein product, the activating transcription factor ATF3 belongs to an ‘expanded’ family of basic leucine zipper (bZIP) domain containing AP-1 transcription factors[36–38] that bind to the promoters of genes under both basal and stress-induced conditions to regulate their expression[37]. We hence tested if ATF3 protein levels are induced under our tested conditions, as these treatments concomitantly reduce nascent protein synthesis rates in cells (Figure 4d, Extended Data Figures 8a–b). To address this paradox, we determined that *ATF3* mRNA escapes the imposed translation block and ATF3 accumulates in the nucleus of cells, concordant with its role as a transcription factor. We observed a striking accumulation of ATF3 with the WT but not the *ΔdotA* strains during infection (Figure 5f, Extended Data Figure 7b). Infections with

Δ5 L.p. or an isogenic *ΔsidI L.p.* strain[5] failed to induce ATF3 accumulation (Figure 5f, Extended Data Figure 7c). Importantly, complementing these *L.p.* strains with plasmids encoding *sidI* restored their ability to induce ATF3 (Figure 5f, Extended Data Figure 7c). ATF3 accumulation was also observed with the expression of FLAG-SidI but not the other *L.p.* EITs, nor the enzymatic deficient mutant FLAG-SidI R453P (Figure 5g), and with cells treated with mild doses of ANS, DD-B and DON, but not CHX and HTN (Extended Data Figures 7i–j). By indirect immunofluorescence and confocal microscopy analyses, we visualized the translocation of ATF3 from the cytosol in control cells to the nucleus in cells that were infected with the WT and the *Δ5+sidI L.p.* strains (Figure 5h; arrows), as well as in cells treated with ANS, DD-B or DON (Extended Data Figure 7k; arrows). ATF3, however, remained diffuse in cells infected with the *ΔdotA, Δ5* and *Δ5+lgt1* strains (Figure 5h). Taken together, our results suggest that cells, in response to ribosome stalling and collisions, activate a conserved stress signature that results in the accumulation of ATF3 in the nucleus.

Collided ribosome stress signals to activate ATF3 accumulation

Since ribosome stalling has been linked to the activation of the ISR and RSR pathways[12,16,29], we asked which of these pathways regulate the increase in ATF3. First, we challenged mouse embryonic fibroblasts (MEFs) that carried either the wild type eIF2α S51 alleles (ISR active) or mutant eIF2α S51A alleles (S51 mutated to alanine; ISR null)[39] with ANS for 4 hours and assayed for ATF3, ATF4 and eIF2α phosphorylation by immunoblotting. As controls, we treated cells with the ISR activator thapsigargin (Tg) for 4 hours[40,41]. In accordance with published studies[41], Tg activated the accumulation of both ATF3 and ATF4 in ISR active but not ISR-null MEFs (Extended Data Figure 8c).

Surprisingly, mild ANS doses induced a marked accumulation of ATF3 in both ISR active and ISR-null MEFs, while ATF4 accumulation was entirely absent (Extended Data Figure 8c). ATF3 accumulation also occurred when MEFs were challenged with mild doses of DD-B, with a more pronounced increase of ATF3 in the ISR null MEF cells (Extended Data Figure 8d). Furthermore, treatment of HEK293T cells with the ISR inhibitor ISRIB[42] also failed to suppress the increases of ATF3 when these cells were treated with ANS or transfected with FLAG-SidI (Extended Data Figure 8e). In sum, these results argue against a role for the ISR pathway to enable ATF3 accumulation in response to ribosome stalls.

We then tested if ATF3 accumulation is dependent on the RSR pathway. Our treatment regimen of ANS, DD-B and DON in HEK293T cells strongly activated p38 phosphorylation (p-p38), while corresponding treatments with CHX and HTN did not (Extended Data Figure 8f–g). We also detected similar increases of p-p38 and ATF3 in HeLa cells treated with a mild dose of ANS, DD-B and DON (Figure 6a). Depleting these cells of ZAK (ZAK knockdown (KD)) with small interfering RNA (siRNA) suppressed the drug induced increases of both p-p38 and ATF3. Concordantly, p38 depletion with siRNA (p38 KD) also significantly inhibited the accumulation of ATF3 (Figure 6a). These results suggested that ZAKα is the upstream kinase that phosphorylates p38 to regulate ATF3 induction.

In line with these findings, FLAG-SidI expression in HEK293T cells also activated a marked increase in p-p38 levels, similar to the intensity elicited by ANS and DD-B treatments and

dependent on SidI's glycosyl transferase activity (Figure 6b). Furthermore, the expression of only SidI but not the other *L.p.* EITs strongly activated p38 phosphorylation in HEK293T cells (Figure 6c).

In an *L.p.* infection context, global phosphoproteomics analyses in HEK293-FcγR cells from our lab[43-preprint] indicated that, as early as one hour post infection, *L.p.* induced a significant activation of the stress activated protein kinase pathway in infected cells, as determined by an enrichment of substrates phosphorylated by the stress kinases p38α, p38β and MAPKAP2 (MK2) (Extended Data Figure 8h, Supplementary Table 6). This result is supported by previous data suggesting that p38 is activated after WT *L.p.*[44], but not *Δ5 L.p.* infection[10]. We confirmed and expanded on these results by determining that *L.p.* robustly induced the phosphorylation and activation of p38 (p-p38) and ZAKα (high molecular weight species; p-ZAK) in infected cells (Figure 6d; lanes 1 and 2). p38 activation in infected cells was largely dependent on the secretion of SidI by *L.p.* (Extended Data Figure 8i). Furthermore, cells depleted of ZAKα and p38 by siRNAs or treated with small molecule inhibitors of ZAK[45] and p38 kinases failed to accumulate ATF3 in response to a *L.p.* challenge (Figures 6d–f). We surmise from these data that p38 signaling in *L.p.* infected cells primarily initiates from collided ribosomes and that the RSR regulates ATF3 accumulation (Figure 6g).

Cis-acting determinants on *ATF3* mRNA regulate its translation

Using a targeted ribosome profiling strategy (Figure 6h), we observed that in unstressed cells, *ATF3* mRNA, along with the transcripts *ODC1, RPS29* and *HPRT*, that encode for 'house-keeping' proteins, exhibit an enriched association with polysomes, with little to no detection of these transcripts in either the RNP or the 80S fractions (Figure 6i). Importantly, in cells treated with a mild 0.1μM ANS dose or expressing FLAG-SidI, all four mRNAs exhibited a reduction in polysome association with a more pronounced effect in cells expressing FLAG-SidI (Figure 6i), indicative of translation elongation defects. However, strikingly, when the abundance of polysome-bound *ATF3* mRNA was quantitated relative to the abundances of either *ODC1*, *RPS29* or *HPRT* in the same fractions, *ATF3* mRNA remained significantly enriched (~ four- to six-fold higher) only in polysome fractions profiled from cells treated with ANS or expressing FLAG-SidI (Figure 6j). These results suggest that while translation stalling occurs across transcripts during colliding ribosome stress induction, *ATF3* mRNA still associates abundantly with ribosome populations that potentially remain translationally active in cells. To test whether actively translating ribosomes are essential for ATF3 accumulation during stress, we blocked translation with CHX or HTN either before (PRE) or after (POST) treatment with ANS, DD-B or FLAG-SidI and assayed for ATF3 accumulation by immunoblotting. In strong support of our hypothesis, CHX and HTN under both treatment regimen suppressed ATF3 accumulation (Figure 6k), indicating that the translation of *ATF3* during the RSR requires an active pool of initiating and elongating ribosomes.

In further support of this notion, cells either treated with a mild ANS dose or expressing FLAG-SidI activated the striking induction of a fluorescent mApple reporter driven by a 399 bp optimized sequence of the 5'-UTR of *ATF3* that includes the first 95 bp of exon 2 of the

main *ATF3* coding sequence and encodes a putative upstream open reading frame (uORF) (Figure 6l, Methods). Surprisingly, mApple expression in cells still remained induced when the AUG start codon in the uORF was altered to AGG (Figure 6m). Complementing these findings, as further controls, ANS treatments or FLAG-SidI expression failed to induce mApple expression driven by a gene sequence containing uORF1 and uORF2 of *ATF4* mRNA (Figure 6n).

Together, these results indicate that during colliding ribosome stress, *ATF3* mRNA remains tightly associated with a pool of translating polysomes and cis-regulatory features in the 5'-UTR of *ATF3* mRNA enable its preferential translation.

ATF3 orchestrates a transcriptional program that regulates cell fate

We next focused on understanding the significance of the stress-induced ATF3 accumulation in cells. Upon mining genome-wide chromatin immunoprecipitation and sequencing (ChIP-seq) datasets collected from four diverse cell types, we found that ATF3 bound to euchromatin rich genomic regions in one or more cell type (marked by acetylated histone H3K27Ac), at or near the exons of genes coding for its own mRNA, as well as the mRNAs of *TNFRSF12A*, *HSPB8*, *PPP1R15A* and *GADD45A* (Extended Data Figure 9).

Prompted by this observation, we challenged ATF3 knockout (KO) cells (Figures 7a–b) and the isogenic HEK293T parental cells with FLAG-SidI, FLAG-SidI R453P or a mild ANS dose and assayed for the mRNA levels of the four stress-inducible transcripts by qRT-PCR. As expected, FLAG-SidI expression and ANS treatment led to a strong induction in the mRNA levels of all four genes in the parental cell line (Extended Data Figure 10a–d). In ATF3 KO cells, however, stress transcript induction was attenuated (Extended Data Figure 10a–d; ATF3 KO panels). Importantly, the expression of an enzymatically deficient SidI mutant (FLAG-SidI R453P) in both cell lines failed to activate mRNA induction (Extended Data Figure 10a–d).

We then monitored the viability of parental and ATF3 KO cells expressing GFP, FLAG-SidI or FLAG-SidI R453P for three days (Figure 7c). In both cell types, GFP expression did not interfere with cell growth, with a progressive doubling of viable cells that plateaued at day 3 post-transfection. FLAG-SidI R453P expression resulted in similar rates of cell growth in both parental and ATF3 KO cells, but at slower rates when compared to GFP expressing cells. In contrast, FLAG-SidI expression in parental 293T cells resulted in a severe reduction of viability at days 2 and 3 post transfection. However, a depletion of ATF3 rescued cell viability in cells expressing FLAG-SidI, with these ATF3 KO cells mirroring the growth rates observed with cells expressing the enzymatic deficient mutant SidI R453P. In sum, these results indicate that (i) SidI has a cytopathic effect on cellular growth via ATF3; (ii) in the absence of ATF3, SidI causes cytostasis; and (iii) enzymatically defective SidI also causes cytostasis independent of ATF3 function, likely due to its inhibitory effect on protein synthesis (see Figure 3d).

Finally, we tested the role of ATF3 during *L.p.* infections in HEK293-FcγR cells. Challenging these cells for up to 10 hours with a large pathogenic burden (multiplicity

of infection = 50) of WT *L.p* resulted in significant reduction of cell viability only at late stages of infection as compared to uninfected controls (Extended Data Figure 8j, Figure 7d–f). This result suggested that such high amounts of *L.p.* replicating for ten hours would recapitulate the final stages of its intracellular replication cycle that ultimately leads to cell lysis[46–48]. In contrast, challenging cells with either the *ΔdotA L.p.* or *Δ5 L.p.* resulted in minimal cell death (Figure 7d). Strikingly, infecting cells with the complemented *Δ5+sidI L.p.* strain caused a similar reduction of cell viability to that observed during infections with WT *L.p.* (Figure 7d), indicating that the secretion of SidI by *L.p.* is sufficient for this phenomenon. We then either depleted ATF3 with siRNAs (Figure 7e; blot) or inhibited the ZAK and p38 kinases with small molecule inhibitors (Figure 7f) in HEK293-FcγR cells and challenged these cells with WT *L.p.* for 10 hours. Indeed, in control cells, WT *L.p.* led to an almost fifty percent reduction in the number of viable cells when compared to uninfected controls (Figure 7e–f). In contrast, in cells depleted for ATF3 or treated with ZAK and p38 inhibitors, WT *L.p.* infections failed to significantly reduce cell viability (Figure 7e–f), underscoring the notion that ATF3 accumulation downstream of RSR pathway activation during *L.p.* infections triggers a terminal program that regulates cell fate.

Discussion

We report the discovery of an unprecedented secreted bacterial effector toxin SidI with a tRNA-like shape and glycosyl transferase activity that targets the host translation machinery to induce ribosome collisions, thereby activating a ribotoxic stress response. Via this mechanism, *L.p.* appropriates a ribosome-to-nuclear stress-signaling pathway that regulates cell fate.

Mechanistically, the bipartite targeting and enzymatic capabilities of SidI mirror the mode of action exhibited by the toxin ricin, a heterodimeric ribosome-inactivating protein whose galactose binding B-chain enables targeting and uptake by cells and whose enzymatic A-chain functions as an N-glycoside hydrolase that depurinates adenine on the sarcin/ricin loop of 28S ribosomal RNA[17,49]. SidI similarly requires an active enzymatic domain to potently inhibit protein synthesis in the picomolar range (Figure 1b–c, 3d–e).

To our surprise, and in striking contrast to ricin, SidI mediated protein synthesis inhibition also occurs efficiently in *E.coli* S30 extracts supplemented with GDP-mannose (Figure 3g). Interestingly, *L.p.* encodes a meta-effector of SidI named MesI to counteract the effects elicited by SidI[50]. MesI directly binds to SidI inside bacterial cells[51] and inhibit its GDP hydrolysis activity[8]. Indeed, *L.p.* mutants with a genomic deletion of the *mesI* locus fail to replicate intracellularly[50,51], likely due to the cytotoxic effect associated with SidI activity that is unrestricted due to the absence of its dedicated anti-toxin MesI.

Multiple lines of evidence indicate that SidI likely interferes with an early step of the translation elongation cycle. First, SidI co-sediments with actively translating ribosomes (Figure 1g), directly interacts with ribosomes (Figures 3b–c) and mannosylates ribosomes at or near the A-site/P-site (Figure 4a–c, Extended Data Figure 4d–f). Second, the expression of SidI in cells induces ribosome stalling and collisions in a manner that is dependent on its mannosyl transferase activity (Figure 4d–f). Third, SidI activates a RSR signature

in cells that is exceptionally similar to one activated by ANS, DD-B and DON that interfere with A-site function[32,35], but not CHX, that occupies the E-site and inhibits tRNA translocation[35] (Figures 5–7, Extended Data Figures 7d–k, 8f–g). Con-A pulldowns of ribosomes enzymatically modified by SidI enriched for uL3 and uL2 that form essential structural contacts with ribosomal RNA in the peptidyl transferase center (PTC); uL4 that is an integral part of the peptide exit tunnel and contains an unstructured segment buried in the vicinity of the PTC; and uL13 that regulates the function of the GTPase associated center (Extended Data Figure 4d–f). Studies have shown that either mutations or small molecule drugs that abrogate the function of these ribosomal proteins strongly impacts translation elongation and inhibits protein synthesis[52–59]. These findings support a mechanism wherein SidI mannosylates ribosomes to block either tRNA loading onto the A-site or the peptidyl transferase reaction at the A-site/P-site interface to induce ribosome stalling and inhibit protein synthesis.

As a consequence, in cells challenged with *L.p.*, SidI secreted into the cytosol induces a ZAKα→p38→ATF3 dependent ribotoxic stress response (RSR). While we cannot completely rule out an inhibition of degradative mechanisms that regulate ATF3 protein turnover[60,61], our data support a model wherein cis-regulatory determinants on the 5'-UTR of the *ATF3* mRNA enable this transcript to associate significantly with a pool of translating ribosomes (Figure 6h–n). Indeed, during *L.p.* infections, the 5'-UTRs of a few transcripts have been shown to regulate their translation[34]. Notably, ATF3 functions as a master transcription factor of the RSR pathway and regulates the activation of a cell death program, presumably via modulating gene expression in stressed cells (Extended Data Figures 9–10). These findings complement other studies on host directed gene expression induced by low dose challenges of *L.p.* in macrophages[34,62] and the amoeba *Dictyostelium discoideum*[63,64]. Macrophages exhibit an RSR-like signature[34] (Extended Data Figure 7a), accumulate ATF3 (Extended Data Figure 7b), and undergo lysis at late stages of infection[46–48]. Although HEK293 FcγR cells recapitulate these major steps of the infection process, the mechanisms that regulate the cell viability of *L.p.* infected macrophages are likely more complex and are influenced by a combination of signals from inflammatory and non-inflammatory inputs[48,62,65,66]. On the other hand, *D. discoideum* fails to elicit a canonical RSR[63,64]. This is not surprising as the expression of ATF3 and its homologues is restricted to higher vertebrate organisms. Interestingly, however, *D. discoideum* cells activate a gene expression program that largely impacts the protein synthesis machinery, with an upregulation of transcripts coding for multiple tRNA ligases and a downregulation of transcripts coding for ribosomal proteins[63,64]. These changes potentially highlight a more primitive response to translation stress induced by *L.p.* in these lower organisms.

We propose that high intracellular bacterial loads of *L.p.* induce a ribosome collision rate that results in the induction of the RSR pathway. As SidI is largely dispensable for the intracellular replication of *L.p.* in macrophages[3], our results point to a model wherein *L.p.*, via SidI, selectively hijacks the RSR pathway to activate the terminal program of cell lysis at late stages of infection once bacterial replication is complete (Figure 7g). This process likely aids *L.p.*'s egress from the host cell. Our study expands the portfolio of stress response pathway regulators derived from *L.p.*, underscoring *L.p.*'s amazing utility as

a molecular tool box to uncover mechanistic angles and fundamental aspects of host cell physiology[2,6,27,67–71].

Methods

Cell lines and cell culture:

HEK293T (ATCC, CRL-3216), HEK-293 FcγR (Kind gift from Craig Roy, Yale University), HeLa (ATCC, CCL-2), MEFs (Kind gift from Randal J.Kaufman, Sanford Burnham Prebys Medical Research Institute) and primary BMDM cells[72] were cultured in DMEM-high glutamine media. K562 cells (Kind gift from Jonathan Weissman, Broad Institute, MIT; RRID:CVCL_0004) were cultured in RPMI-high glutamine media. Both DMEM and RPMI were supplemented with 10% fetal bovine serum (FBS) and the cells were maintained at 37 °C and 5% CO_2. For the MEF cell cultures, DMEM media was further supplemented with penicillin-streptomycin antibiotic, sodium pyruvate and non-essential amino acid mixtures. For the primary BMDM cultures, DMEM media was supplemented with 20% FBS, 10% recombinant M-CSF, glutamine, sodium pyruvate and penicillin-streptomycin antibiotic. HEK293T and HEK-293 FcγR cells were seeded in poly-L-lysine–treated plates. Cells were grown to ~75 to ~90% confluency for most experiments. Each cell line was routinely screened for mycoplasma contamination using the MycoScope™ PCR Mycoplasma Detection Kit (Genlantis Cat#MY01050). The cell lines from ATCC were authenticated by STR profiling. The cell lines that were kind gifts from researchers were not authenticated.

Preparation of recombinant EIT DNA:

L.p. genes were amplified from *L.p.* (Lp01) genomic DNA by PCR and cloned into respective vectors. For mutagenesis, Q5 site directed mutagenesis kit (NEB) was used and the manufacturer's instructions were followed.

Recombinant protein purification:

E. coli BL21 (DE3) cultures expressing pGEX6P1 plasmids were first grown overnight at 37°C. These overnight cultures were then sub-cultured at 1:100 in LB supplemented with the appropriate antibiotics until OD_{600} values reached 0.6. This was followed by the induction of protein expression with 1 mM IPTG and the bacteria were cultured at 16°C overnight. The next day, bacterial cultures were centrifuged at 6000 rpm for 5 min at 4°C followed by incubation of pellets in bacterial lysis buffer [50 mM Tris pH 8, 100 mM NaCl, 1 mM ethylenediaminetetraacetic acid (EDTA), 200μg/mL lysozyme, 2 mM dithiothreitol (DTT), 10μg/mL DNase, and complete protease inhibitor] for 60 minutes on ice. The mixtures were then sonicated on ice [pulse on 30 seconds; pulse off 10 seconds – 30% amplitude for 5 minutes] and centrifuged at 15,000 g for 30 min at 4°C. The supernatant fractions were incubated with glutathione coupled sepharose beads overnight at 4°C with rotation. The beads were then transferred to a 20mL Maxi column with rubber stoppers and washed with 5 column volumes of wash buffer I (PBS, 0.05% Triton X-100, 1mM DTT), followed by wash buffer II (PBS, 0.05% Triton X-100, 0.5M NaCl, 1mM DTT). The GST-tagged proteins were then eluted with elution buffer (50 mM Tris pH 7.5, 150mM NaCl, 10 mM glutathione, 1mM DTT) and concentrated with Amicon Ultra centrifugal filters at 4°C with repeated

mixing to prevent aggregate formation. Purified proteins were visualized by SDS-PAGE and Coomassie brilliant blue staining. Protein concentrations (in μM) were calculated by the Beer-Lambert equation A = εlc where A is the absorbance of the protein in solution at 280nM, ε is the calculated extinction coefficient of the protein based on its amino acid sequence, l is the light path length and c is the concentration of the protein in solution. The extinction coefficients used for calculations of GST-tagged proteins are as follows: GST-SidI (ext. coeff. = 125335); GST-Lgt2 (ext. coeff. = 113065); GST-SidL (ext. coeff. = 93920); GST-Δ1–58-LegK4 (ext. coeff. = 122270); GST-RavX (ext. coeff. = 62270). In certain cases, proteins were further purified by gel filtration chromatography using a Superdex 200 column attached to an AKTA-format FPLC (GE Healthcare) and running buffer containing 50mM Tris pH 7.5, 150mM NaCl and protease inhibitor cocktail. Elution fractions containing protein were analyzed by their A_{280} spectra, SDS-PAGE and Coomassie brilliant blue staining.

Cell free translation in rabbit reticulocyte lysates:

For each treatment condition, luciferase mRNA (200ng) was translated for 60 minutes at 30°C in reaction mixtures containing nuclease treated rabbit reticulocyte lysates (12.5μL; ~700μg of total protein content), amino acid mixture without leucine (10μM), amino acid mixture without methionine (10μM) and potassium chloride (70mM). By using two incomplete amino acid mixtures, a sufficient concentration of all amino acids is provided. After incubation, the samples were mixed in a 1:1 (v/v) ratio with luciferase assay reagent (Promega) in a 96-well white opaque plate and left at room temperature for 2 minutes. Luminescence readings were then obtained on a BioTek Cytation Imaging reader. The translation efficiency for each condition was calculated as a percentage of the raw luminescence values obtained when reaction mixtures were untreated or treated with GST alone. For the experiments in Figure 3f, rabbit reticulocyte lysates (12.5μL) were first incubated with GST-SidI or GST-SidI R453P for the indicated amounts of time at 30°C. After pre-treatment, amino acid mixtures, potassium chloride and 1μg of luciferase mRNA were added to the tubes and the samples were incubated for a further 60 minutes at 30°C and luminescence values were calculated as described above. In each case, the luminescence values were normalized to values obtained from extracts containing luciferase mRNA and incubated with GST alone for 60 minutes (Control) and expressed as a percentage.

For experiments in Figure 1g and 3c, luciferase mRNA (1μg) was translated for 60 minutes at 30°C in reaction mixtures containing nuclease treated rabbit reticulocyte lysates (100μL), amino acid mixture without leucine (10μM), amino acid mixture without methionine (10μM), potassium chloride (70mM) and GST-SidI/GST-SidI R453P/GST-SidI K-loop mutant (1μM). The translation extracts were then treated with cycloheximide (100 μg/mL) for 5 minutes to freeze polysomes and immediately layered on top of a 10% to 50% sucrose gradient containing 100 mM KCl, 20 mM HEPES (free acid) pH = 7.6, 5 mM $MgCl_2$, 1mM DTT and 100 μg/mL cycloheximide and spun at 160000g for 2 hours at 4°C in a SW-41 swinging bucket rotor. The tubes were then punctured at the bottom with a 16G needle connected to a syringe pump and the lysate was segmented into fractions of ~100μL from the top to the bottom of the tube and collected through a dispenser in each well of a 96 well flat-bottomed plate. Fractions were then pooled together relative to the profile of

the A260 spectra and the proteins in each fraction were extracted with 10% trichloroacetic acid (TCA) and washed with cold acetone. The protein pellets were then incubated with Laemmeli buffer containing beta-mercaptoethanol and boiled for 10 minutes. The denatured proteins were loaded onto an SDS-PAGE gel, transferred onto a nitrocellulose membrane, and immunoblotted for antibodies against GST, uL4 and ueS8.

SidI interactome analyses:

Affinity-precipitation of interactors with glutathione sepharose coupled beads.—HEK293T lysates were prepared using IP lysis buffer (150 mM NaCl, 25mM Tris-HCl pH=7.5, 1% Triton-X and protease cocktail inhibitor from Roche). Rabbit reticulocyte lysates were obtained from Promega. For each experimental replicate, the protein concentrations were quantified and 1mg of total protein lysate was incubated with 1μg/mL of purified GST or GST-SidI overnight at 4°C in a rotary mixer. 25μL of pre-washed glutathione sepahrose beads were added to the samples and the mixtures were incubated for a further 1 hour at 4°C in a rotary mixer. The beads were then washed 5x times with IP lysis buffer to remove any unspecific interactors. The bound interactors were eluted by boiling the beads in Laemmeli buffer containing β-mercaptoethanol and the eluates were run on a 4 – 15 % SDS-PAGE gel. The gels were silver stained (Pierce Silver Stain kit; Thermo Fischer Scientific) and the gel pieces containing prominent protein bands were excised and stored at −80°C for mass spectrometry.

Sample preparation.—25mM NH_4HCO_3/50%Acetonitrile was added to the sample gel pieces after excisions and then dried by vacuum centrifugation. Some samples were reduced by the addition of 15mM TCEP in 25mM NH_4HCO_3, the supernatant removed, and then gel slices were alkylated by the addition of 50mM of chloroacetamide. Other samples were reduced by the addition of 10mM DTT in 25mM NH_4HCO_3, the supernatant was removed, and then alkylation proceeded by the addition of 55mM iodoacetamide in 25mM NH_4HCO_3. Gel slices were washed in 25mM NH_4HCO_3 and then dehydrated in 25mM NH_4HCO_3/50% Acetonitrile. They were then dried by vacuum centrifugation. A solution of 25mM NH_4HCO_3 containing 4ug/mL trypsin was then added to the gel slices and digested overnight at 37°C overnight. The resulting peptides in solution were transferred to a new tube and desalted on C18 spin columns. The eluting peptides were dried by vacuum centrifugation and then resuspended in 0.1% formic acid.

Mass spectrometry data acquisition and analysis.—Samples were injected onto a column (360 μm O.D. × 75 μm I.D., New Objective) packed with 25cm of 1.8 μm Reprosil C18 particles with (Dr. Maisch). Peptides were separated by a reversed-phase gradient using an Easy-nLC 1200 (Thermo Scientific) with mobile phase A consisting of 0.1% formic acid, and mobile phase B consisting of 80% acetonitrile in 0.1% formic acid. Eluting peptides were directly injected into either an Q-Exactive Plus Orbitrap mass spectrometer (Thermo Scientific) or an Exploris 480 Orbitrap mass spectrometer (Thermo Scientific) equipped with a nanospray flex source and operating in positive ion mode. System for both instruments was monitored with QCloud2.On the Q-Exactive Plus mass spectrometer, the total acquisition time was 60 min, MS1 detection was performed in profile mode in the Orbitrap with 70,000 resolution, 300–1500 m/z scan range, 250 ms maximum injection, and an AGC target of

1e6. MS2 fragmentation was performed on charge states greater than 2, with automatic dynamic exclusion, an expected 15s peak width, data collection was in the Oribtrap in centroid mode with 17,500 resolution, 60ms maximum injection time, 5e4 AGC target, 200–2000 m/z scan range, and a 2.0 m/z isolation window and a 26% normalized HCD collision energy. On the Exploris 480 mass spectrometer, the total acquisition time was 60 min, MS1 detection was performed in profile mode in the Orbitrap with 120,000 resolution, 350–1250 m/z scan range, maximum injection time was set to “auto”, and a normalized AGC target of 100%. MS2 fragmentation was performed on charge states 2–6, with 30s dynamic exclusion after 2 occurrences and a +/− 10 ppm window, data collection was in the Oribtrap in profile mode with 15,000 resolution, maximum injection time set to “auto”, 200% normalized AGC target, and a 1.3 m/z isolation window and a 30% normalized HCD collision energy. All raw MS data were searched with MaxQuant (version 2.0.3.0) against the human proteome (Uniprot canonical protein sequences downloaded June 21, 2021) or against the rabbit proteome (*Oryctolagus cuniculus,* downloaded April 6, 2022*)*. Peptides were filtered to 1% false discovery rate in MaxQuant. MaxQuant default parameters were used with the exception that label-free quantification was turned on with match between runs set to 0.7 min. Mass spectrometry data files (raw and search results) have been deposited to the ProteomeXchange Consortium (http://proteomecentral.proteomexchange.org) via the PRIDE partner repository with dataset identifier PXD034240. iBAQ intensity values were used for estimating the relative enrichment of GST-SidI interacting proteins compared to GST-only control samples. After peptide intensities in the eluted pulldown fractions were calculated, datasets were curated by removing any peptides from proteins that are common contaminants in AP-MS procedures and peptides that were enriched in the GST-pulldown eluates (GST-SidI/GST intensity ratio <1) before further analyses.

Purification of ribosomes:

80S Monosomes were purified from K562 cells. A 5ml pellet of K562 cells was resuspended in 3 mL of Lysis Buffer (25 mM HEPES, pH 7.4, 300 mM KOAc, 10 mM $MgOAc_2$, 1 mM DTT, 0.5% NP-40, complete EDTA-free protease inhibitor cocktail (Roche)) and lysed by short intervals of vortexing (10 min). Cell debris were removed by centrifugation for 10 min at 12,000 × g at 4°C and concentration of KOAc was adjusted to 500 mM. Lysate was loaded on a (3:1 v/v) 1M sucrose cushion (25 mM HEPES pH 7.5, 150 mM KOAc, 10 mM $MgOAc_2$, 1 mM DTT, 1 M sucrose and .5 mM PMSF) and centrifuged at 115,800 × g for 15 hrs. The crude ribosomal pellet obtained after the spin was resuspended in buffer (25 mM HEPES pH 7.5, 150 mM KOAc, 10 mM MgOAc, 1 mM DTT, .5 mM PMSF, 1mM EDTA, 1x protease inhibitor cocktail, .2U/mL RNase Inhibitor) and treated with 1 mM puromycin for 15 mins on ice and then 15 mins at 25 C. The 80S monosome fraction and 40S and 60S subunits were then separated by loading onto a 15–30% continuous sucrose gradient (25 mM HEPES, pH 7.4, 500 mM KOAc, 10 mM MgOAc, 1 mM DTT, 1x protease inhibitor cocktail) and centrifuged at 49,500 × g for 18 hrs using a SW40 rotor. Monosomes were pelleted from the suitable fraction by centrifugation at 25,000 rpm for 14.5 hr using a TLA110 rotor. The pellets were suspended in storage buffer (20 mM HEPES, pH7.5, 100 mM KOAc, 10 mM $MgOAc_2$, 1 mM DTT) and stored flash frozen in 10 μl aliquots.

Crude ribosomes were prepared from HEK293T cell extracts. Eight 10 cm dishes of HEK293T cells at 80% confluency were used. After wash with cold PBS twice, cells were collected and resuspended in 1.5 mL cytosol buffer (50 mM HEPES, pH 7.4, 100 mM KOAc, 5 mM Mg(OAc)2, 0.01% digitonin, 40 U/ml Ribonuclease inhibitor (Promega, N2511), 1 mM DTT, and protease inhibitor cocktail), and then disrupted mechanically by passage through a pre-chilled 26G needle using a 10 mL syringe. Cellular debris were cleared by centrifugation at 4°C for 15 min at 12000rpm. The supernatant was collected and the concentrations of KOAc and MgAc2 in the supernatant were increased to 500 mM and 15 mM, respectively. NP-40 detergent was also added to a final concentration of 0.2% to disrupt ribosome-associated proteins. 300μl of sample was then layered over the 1mL sucrose cushion (20 mM HEPES pH 7.4, 500 mM KOAc, 15 mM MgAc2, 0.1 mM EDTA pH 7.4, 1 M sucrose) and centrifuged at 100,000 RPM for 60 minutes at 4°C in a TLA100.3 rotor (Beckman Coulter, 349490) with 3.5 mL polycarbonate tubes (Beckman Coulter, 349622). The supernatant was removed carefully with an aspirator, and the pellets were washed with 100μl ribosome binding buffer (50 mM HEPES, pH 7.4, 100 mM KOAc, 5 mM Mg(OAc)2) [add on top carefully and aspirate; do not disrupt pellet] and resuspended with 30 μl ribosome binding buffer. Before measuring the concentration of ribosomes by A260 with NanoDrop, ribosomes from different tubes were pooled. Ribosomes were aliquoted and flash-frozen in liquid nitrogen and stored at −80°C. The concentration of ribosomes in the extract was calculated by Beer-Lambert equation $A = \varepsilon lc$ where A is the absorbance of the ribosomes at A260, ε is the extinction coefficient of a monosome (4.2×10^7), l is the light path length and c is the concentration of the ribosomes in solution.

In vitro ribosome binding assays:

25μL of glutathione sepharose beads were pre-immobilized with 250nM of GST, GST-SidI, GST-SidI R453P or the GST-SidI K-loop mutant in 100μL of ribosome binding buffer (50mM HEPES, 100mM KOAc, 5mM $MgOAc_2$, 0.1% NP-40) at 4°C for 1 hour and then washed 3x times with ribosome binding buffer. GST/GST-SidI/GST-SidI R453P/GST-SidI K-loop mutant immobilized on beads were then incubated with 50nM of ribosomes in 100μL of ribosome binding buffer at 4°C for 3 hours. The beads were eluted with 30μL of ribosome binding buffer containing 10mM glutathione. The eluates were then subjected to SDS PAGE and immunoblotting with antibodies against 40S or 60S subunit proteins.

GST-tag based affinity-precipitation of proteins from HEK293T lysates:

HEK293T lysates were prepared using IP lysis buffer (150 mM NaCl, 25mM Tris-HCl pH=7.5, 1% Triton-X, 10mM Na3VO4, 40mM β-glycerophosphate, 10mM NaF and protease cocktail inhibitor from Roche). 1mg of total protein lysate was incubated with 1μg/mL of purified GST or GST-SidI overnight at 4°C in a rotary mixer. 25μL of pre-washed glutathione-Sepahrose beads were added to the samples and the mixtures were incubated for a further 1 hour at 4°C in a rotary mixer. The beads were then washed 5x times with IP lysis buffer to remove any unspecific interactors. The bound interactors were eluted by boiling the beads in Laemmeli buffer containing β-mercaptoethanol and the eluates were subjected to SDS-PAGE and immunoblotting with antibodies.

Cryo-EM structure determination of SidI:

Sample preparation for cryo-electron microscopy: For grid freezing, a 3 μl aliquot of 3 μM GST-SidI was applied onto the Quantifoil R 1.2/1/3 400 mesh Gold grid and waited for 30 s. A 0.5 μl aliquot of 0.1% Nonidet P-40 substitute was added immediately before blotting. The entire blotting procedure was performed using Vitrobot (FEI) at 10 °C and 100% humidity.

Electron microscopy data collection: Cryo-EM data was collected on a Titan Krios transmission electron microscope operating at 300 keV. Micrographs were acquired using a Gatan K3 direct electron detector. The total dose was 60 e^{-}/ $Å^2$, and 60 frames were recorded during a 5.7 s exposure. Data was collected at 81,000 × nominal magnification (0.844 Å/pixel at the specimen level), with a nominal defocus range of -1.0 to -2.0 μm.

Cryo-EM image processing: The micrograph frames were aligned using MotionCor2[73] . The contrast transfer function (CTF) parameters were estimated with GCTF[74]. Particles were picked using Gautomatch (developed by Kai Zhang, https://www2.mrc-lmb.cam.ac.uk/research/locally-developed-software/zhang-software/#gauto) without a template. Particles were extracted using a 64-pixel box size and classified in 2D in Relion[75]. Classes that showed clear protein features were selected. Selected particles were then split into three subsets for efficient data processing. Each subclass was subjected to 3D classification (k= 3) and the best was selected. For one of these subsets, particles in the best 3D class were refined to 7.0 Å resolution. These particles were then extracted at a smaller pixel size (0.844 Å) and refined to yield a 4.0 Å reconstruction, which was used as a reference structure for the following steps. Upon obtaining the reference structure, particles from all three subsets were imported to cryoSPARC[76] for homogeneous refinement (using the 4.0 Å reconstruction in Relion as a reference structure) and heterogeneous refinement. The resulting particles from each subset were combined to go through one more round of heterogeneous refinement followed by nonuniform refinement, which results in the final reconstruction at 3.1 Å resolution, consisting of 749 k particles.

Atomic model building, refinement, and visualization: To build the atomic model for SidI, we first performed a structure prediction analysis using RaptorX[77] and found that the C-terminal part of SidI (amino acids 355–865) shared significant homology to a few glycosyl transferase (GT) enzymes, as has been noted previously[8]. Structure prediction analyses did not identify any proteins in the Protein Data Bank database that shared significant homology with the N-terminal part of SidI (amino acids 136–343). We built an atomic model into the EM map of SidI starting from the C-terminal domain using the crystal structure of the *B. subtilis* GT BshA as a template (PDB ID: 5D00)[78]. The predicted structure of SidI C-terminal domain was manually docked into the EM density of SidI and was used as a template for model building. The models were then manually adjusted in Coot[79]. Having built the C-terminal domain, we continued to build the rest of SidI *de novo*. After building SidI, we noticed a small piece of EM density that is not explained by any of the SidI amino acids, and its shape resembles that of a nucleotide. The complete model was then refined in Phenix[80] using global minimization, secondary structure restraints, Ramachandran restraints, and local grid search. Then iterative cycles

of manual rebuilding in Coot and Phenix were performed. The final model statistics were tabulated using Molprobity[81]. Molecular graphics and analyses were performed with the UCSF Chimera package[82]. UCSF Chimera is developed by the Resource for Biocomputing, Visualization, and Informatics and is supported by NIGMS P41-GM103311. The atomic model of SidI has been deposited into PDB (PDB ID: 8JHU) and the EM map has been deposited into EMDB (EMDB ID: EMD-36294). For molecular docking analyses, SidI was manually docked in Chimera onto EEF2 in the EEF2 ribosome complex structure (PDB ID: 6GZ5).

Protein thermal shift assay:

1μM of recombinantly purified GST-SidI, GST-SidI R453P, GST-SidI K600Q, GST-SidI D724N and GST-SidI K-loop mutant was aliquoted into a 384 well plate. 1μL of a 50x stock solution of SYPRO Orange was added to each well and mixed and the volume was made up to 10μL with buffer containing 50 mM Tris pH 7.5, 150mM NaCl and 1mM DTT. Protein melt curves were obtained on a Bio-Rad CFX384 Thermal cycler using the standard met-curve protocol and melting temperature calculations were performed on the CFX Manager software.

Nucleotide-sugar hydrolysis assays:

Recombinantly purified proteins at the indicated concentrations were incubated with nucleotide-sugar precursors (50μM or 100μM) in glycosyl transferase buffer (50mM Tris pH = 7.4, 5mM $MnCl_2$ for assays with UDP-glucose and GDP-mannose; 25mM HEPES pH = 7.5, 2.5mM $MnCl_2$ for assays with GDP-fucose). For experiments in Figure 4a, crude ribosome extracts were added to the reaction mixtures. All samples were then incubated at 37°C for 60 minutes. After incubation, the samples were mixed in a 1:1 (v/v) ratio with nucleotide detection reagent (Promega) in a 96-well white opaque plate and left at room temperature in the dark for another 60 minutes. The addition of the nucleotide detection reagent quenches the glycosyl transferase reaction. Luminescence readings were then obtained on a BioTek Cytation Imaging reader. To measure nucleotide release for each experiment, raw luminescence values obtained by treating serial dilutions of pure UDP or GDP (Promega) with the nucleotide detection reagent for 60 minutes were used to plot a standard concentration curve. The slope of the standard curve was then used to calculate the amount of nucleotide hydrolysed under different treatment conditions.

In vitro mannosylation assay with radiolabelled GDP-H^3-mannose and scintillation counting:

Recombinantly purified GST-SidI and GST-SidI R453P at the indicated concentrations were incubated with radiolabelled GDP-H^3-mannose (1.25nM) alone or together with purified ribosomes (30nM) in RNC buffer supplemented with 5mM $MnCl_2$. All samples were then incubated at 37°C for 60 minutes. The volume of the samples was made up to 100μL with RNC buffer and 25μL of glutathione Sepharose beads were added to each sample. The samples were incubated in a rocker for 60 minutes. The beads were washed 3x times with RNC buffer and eluted with 50μL of RNC buffer containing 10mM glutathione. The eluates were then subjected to liquid scintillation counting on a Beckman LS 6000IC scintillation counter. The counts per million (cpm) of H^3-mannose labelled moieties in

reactions containing GST-SidI were normalized to the cpm values in reactions containing GST-SidI R453P and the results were plotted as a fold change in H^3-mannose labelling.

In vitro mannosylation and Concanavalin A pulldown:

1.4μM of recombinantly purified GST, GST-SidI or GST-SidI R453P were incubated with or without 1mM of GDP-mannose and 30nM of ribosome extracts in RNC buffer supplemented with 5mM $MnCl_2$ at 37°C for 60 minutes. 25μL of Concanavalin-A Sepharose beads were washed with RNC buffer containing 0.2% NP-40 and the washed beads were added to the samples and incubated at 4°C for 3 hours in a rotary mixer. The beads were then washed 3x times with RNC buffer and bound mannosylated molecules were eluted with RNC buffer containing 200mM methyl-α-D-mannopyranoside (Sigma-Aldrich, M6882). The eluted fractions were then subjected to SDS-PAGE and immunoblotting with antibodies.

In vitro mannosylation followed by Concanavalin-A pulldown coupled to mass spectrometry:

In vitro mannosylation, tryptic digestion and Con-A enrichment of peptides: 1μM of recombinantly purified GST-SidI or GST-SidI R453P was incubated with 240nM of purified ribosomes in duplicates in RNC buffer supplemented with 5mM $MnCl_2$ at 37°C for 60 minutes. The samples were denatured with 8M urea (pH = 8) in 25mM ammonium bicarbonate (ABC), reduced with 5mM DTT in ABC and incubated at 60°C for 30 minutes. The samples were allowed to cool, and then alkylated with 15mM of iodoacetamide in ABC, vortexed and allowed to incubate in the dark at room temperature for 45 minutes. DTT was then added to stop alkylation. ABC solution was added to the samples such that the pH reached 8/8.5. 200ng of sequencing grade trypsin was added to the samples and they were incubated at 37°C for 4 hours with constant rotation. 20μL of Con-A Sepharose beads was added to each sample and they were incubated at 4°C overnight with constant rotation. The beads were washed with excess (500μL) of cold 25mM ABC at 4°C to remove unbound peptides. Mannosylated peptides were eluted with 200mM methyl alpha-D-mannopyranoside in 25mM of ice-cold ABC buffer. 10μL of 10% formic acid was added to the eluates for desalting.

LC-MS/MS: The tryptic peptides were desalted with u-C18 ZipTips (Millipore), and then analyzed using on-line liquid chromatography with tandem mass spectrometry. Specifically, an Orbitrap Fusion Lumos Mass Spectrometer (Thermo Scientific) was coupled to a NanoAcquity UPLC system (Waters). The solvents were 0.1% formic acid in water (A) and 0.1% formic acid in acetonitrile (B). Sample was separated on an Easy-Spray HPLC column (75 μm × 150 mm, Thermo Scientific) using a linear gradient from 5% to 30% B over 72 minutes at 400 nl / min, then 30% to 50% B over 2 mins. For the data-dependent MS/MS acquisition, the precursor ions were measured in the orbitrap with a resolution of 120000 FWHM between 350–1800 m/z (Cycle Time: 3s, Max Injection Time: 50 ms, Intensity Threshold: 5e4). The fragment ions produced by hybrid fragmentation mode EThcD were detected in the orbitrap with a resolution of 30000 FWHM (Collision Energy: 25%, Quadrupole Isolation Window: 1.6m/z, Max Injection Time: 250 ms).

LC-MS/MS Data Analysis: The acquired raw data was converted into peaklists using in-house PAVA software, then analyzed using Protein Prospector (v6.3.23). Spectra were searched against a combination of human and Canavalia brasiliensis proteins from SwissProt downloaded June 2021 (26402 entries), the user-defined sequence of SidI, plus sequence randomized versions of these entries to allow false discovery rate (FDR) estimation. Full tryptic specificity was required and precursor and fragment tolerances of +/− 5ppm and 20ppm, respectively, were employed. Quantification was performed using Protein Prospector by extracting peak intensities of identified peptides. Results were thresholded to an estimated 1% FDR at the unique peptide level. The peptides were subjected to automated screening for standard modifications such as carbamidomethylation of cysteines, protein N-terminal acetylation, pyroglutamate formation from peptide N-terminal glutamine, pyro-carbamidomethyl cysteine from peptide N-terminal cysteine, methionine oxidation, and hexose modification of serines, threonines or lysines. Mass spectrometry data files (raw and search results) have been deposited to the MassIVE repository with dataset identifier MSV000091992. Stringent criteria was adopted to analyse our mass spectrometry dataset by first selecting for proteins enriched by Con-A whose peptide count was ≥ 2 in each replicate of the enzymatic reactions containing GST-SidI. We then further selected for proteins that were either uniquely detected or had a >2.5-fold higher average peptide count after Con-A pulldowns of the enzymatic reactions containing GST-SidI as compared to reactions containing the enzymatic mutant GST-SidI R453P.

Visualization: Con-A enriched ribosomal proteins were mapped in Chimera onto the ribosome structure with P-site and E-site tRNAs highlighted (PDB ID: 6GZ5). SidI was manually docked onto the structure and represented as a mask (orange).

Bacterial strains and infection protocol:

All *L.p.* strains are mentioned in the Key Resources Table. *L.p.* infections were performed as previously described[6,27,67,68]. *L.p.* strains were grown on charcoal yeast extract (CYE) agar plates supplemented with iron ($FeNO_3$ 0.135g/10mL) and cysteine (0.4g/10mL). Chloramphenicol (10μg/mL), IPTG (0.1mM), and thymidine (100μg/mL) were added to CYE agar plates as needed. For infection experiments, primary patches of *L.p.* were grown for 2 days at 37°C on CYE plates. Single colonies of bacteria were picked and grown as heavy patches for 2 further days on CYE plates at 37°C. Heavy patches were then harvested, diluted in AYE broth supplemented with the required chemicals (as appropriate) and grown overnight at 37°C with shaking (220rpm) until the OD_{600} = ~3. HEK293 FcγR cells were infected at a multiplicity of infection (MOI) of 50 or 5. For opsonization, *L.p.* bacteria were diluted in complete media and mixed with a *Legionella* polyclonal antibody (Invitrogen, Cat #PA1–7227) at 1:1,000 dilution. The mixtures were then incubated for 20 minutes at room temperature in a rotary mixer. Immediately after addition of the opsonized *L.p.* mixtures, cells were centrifuged for 5 min at 1,000 rpm to facilitate spin-fection. Cells were then incubated at 37 °C for 60 minutes to allow bacterial uptake via the FcγR. After 60 minutes, the cells were washed with 1x PBS to remove extracellular bacteria and replenished with DMEM supplemented with 10% FBS. Infected cells were then cultured at 37 °C until time of harvest.

Transfection:

HEK293T cells were transfected with plasmid vectors using the TransIT-TKO Transfection Reagent. siRNA treatments in HeLa and HEK293 FcγR cells were carried out using a pool of siRNAs and Lipofectamine 2000. Expression or knockdown efficiencies (>85%) were checked after every experiment by immunoblotting. Each individual siRNA in the pool was also tested for knockdown efficiency with similar results. A list of siRNA sequences used in this study can be found in Supplementary Table 7.

RNA extraction and quantitative real time PCR:

RNA isolation was performed using the Direct-zol™ RNA Miniprep Plus kit (Zymo Research) according to the manufacturers protocols. The yield and the integrity of RNA were determined by spectrophotometer NanoDrop 2000c For qRT PCR analyses, 1μg of RNA was converted to cDNA using the QuantiTect Reverse Transcription Kit (Qiagen). Quantitative real time PCR reactions were performed with cDNA using iTaq Universal SYBR Green supermix (Bio-Rad) in 384 well plates and 500nM of forward and reverse primers on a Bio-Rad CFX384 Thermal cycler. The fold changes in the relative quantifications were calculated according to the ΔΔCt method. See Supplementary Table 7 for a list of qRT-PCR primers.

Puromycin-pulse chase assays:

Cells were treated with 2μg/mL puromycin for 10 minutes followed by puromycin wash out with PBS. Cells were then chased with complete medium for 50 minutes, washed with PBS and lysed with RIPA buffer. The lysates were then subjected to immunoblotting. For cells infected with *L.p.*, chloramphenicol (25 μg/mL) was added 15 minutes prior to puromycin addition to inhibit bacterial translation.

Cell extract preparation and immunoblotting:

Cells were washed three times with PBS and collected immediately at 4°C in RIPA lysis buffer containing phosphatase inhibitors (1% Triton X-100, 20mM Tris-HCl, pH 8.0, 0.1% SDS, 0.05% sodium deoxycholate, 150mM NaCl, 10mM Na3VO4, 40mM β-glycerophosphate, 10mM NaF) and complete protease inhibitors (5×; Roche). The detergent soluble supernatant fractions were immediately processed for SDS–PAGE and immunoblotting with antibodies.

Polysome profiling:

HEK293T cells grown in 10cm plates were transfected with constructs expressing GFP, FLAG-SidI or FLAG-SidI R453P for 24 hours. Cells were then treated with cycloheximide (100 μg/mL) by adding it to the media for 5 minutes before harvesting. Cells were washed with ~5ml ice cold PBS + cycloheximide and spun at 16000g for 1 minute at 4°C. The pellet fraction was resuspended in lysis buffer (10 mM HEPES pH = 7.9, 1.5 mM $MgCl_2$, 10 mM KCl, 0.5 mM DTT, 1% Triton X-100, 100 ug/ml cycloheximide). The cells were incubated for 10 minutes on ice to allow swelling. Cells were then triturated ten times through a pre-chilled 26G needle and the debris were spun at 1500 g for 5 minutes at 4°C to pellet nuclei. The supernatant fraction of the lysate was then flash frozen and stored at −80°C if

required. 200 µl of lysate was layered on top of a 10% to 50% sucrose gradient containing 100 mM KCl, 20 mM HEPES (free acid) pH = 7.6, 5 mM $MgCl_2$, 1mM DTT and 100 µg/mL cycloheximide and spun at 16,000g for 2 hours at 4°C in a SW-41 swinging bucket rotor. The tubes were then punctured at the bottom with a 16G needle connected to a syringe pump and ribosome populations across the gradient were analysed by measuring absorbance values at 254nm using a spectrophotometer.

For experiments monitoring ribosome collisions, cells were rinsed with ice cold PBS and the cell pellet was lysed in 200µL of lysis buffer (20mM Tris-Cl pH = 8, 150mM KCl, 15mM MgCl2, 1% Triton X-100, 1mM DTT, and EDTA-free Protease inhibitor cocktail). The entire lysate pool for each condition were treated with RNase-A at 4 µg/mL for 15 min at room temperature in a rotary shaker and immediately run through 10%–35% sucrose gradients (20 mM Tris-Cl pH = 8, 150 mM NaCl, 5 mM MgCl2) using Beckmann Coulter SW41 Ti rotors at 200000g for 4°C for 2 hr.

For Figure 6i, *ATF3* mRNA association with ribosomes in cells was contrasted against the association of three distinct mRNAs whose protein products perform cellular house-keeping functions – ODC1 (coding for ornithine decarboxylase), RPS29 (coding for the ribosomal protein RPS29) and HPRT (coding for hypoxanthine-guanine-xanthine phosphoribosyltransferase). Lysates were collected from unstressed cells, cells treated with a mild 0.1µM ANS dose for 4 hours, or cells expressing FLAG-SidI for 16 hours and run on increasing 10% to 50% sucrose gradients at high speed to sediment ribosome populations. RNA was extracted from three main fractions corresponding to the low molecular weight ribonucleoprotein (RNP)/40S/60S pool, the 80S monosome pool (1 ribosome per mRNA) and the high molecular weight polysome pool (≥ 2 ribosomes per mRNA). Sequential fractions of ~100µL from the top to the bottom of the tube were collected through a dispenser in each well of a 96 well flat-bottomed plate. Fractions corresponding to the RNP/40S/60S, 80S and polysomes were then pooled together relative to the profile of the A260 spectra and the RNA in each fraction was preserved by adding an equal volume of Trizol reagent. RNA isolation was performed using the Direct-zol™ RNA Miniprep Plus kit (Zymo Research) according to the manufacturers protocols. The yield and the integrity of RNA were determined by spectrophotometer NanoDrop 2000c. For qRT PCR analyses, RNA was converted to cDNA using the QuantiTect Reverse Transcription Kit (Qiagen). Quantitative real time PCR reactions were performed with cDNA using iTaq Universal SYBR Green supermix (Bio-Rad) in 384 well plates and 500nM of forward and reverse primers on a Bio-Rad CFX384 Thermal cycler. The relative mRNA percent in each fraction was calculated as previously described[83]:

$$\Delta Ct_{fraction(x)} = Ct_{fraction(x)} - Ct_{fraction(RNP/40\,S/60\,S)}$$

$$\%mRNA = 100*[2^{-\Delta Ct\ fraction(x)}/(2^{-\Delta Ct\ fraction(RNP/40S/60S)} + 2^{-\Delta Ct\ fraction(monosome)} + 2^{-\Delta Ct\ fraction(polysome)})]$$

X = fraction where % mRNA is to be calculated .

For Figure 6j, the fold changes in mRNA association in the polysome fractions were calculated according to the ΔΔCt method. The abundance of *ATF3* mRNA was first normalized to either *ODC1*, *RPS29* or *HPRT* (ΔCt). The ΔCt values in ANS and FLAG-SidI conditions were then normalized to those obtained in unstressed (control) cells (ΔΔCt). Fold change was calculated with the formula $2^{-\Delta\Delta Ct}$. See Supplementary Table 7 for a list of qRT-PCR primers.

RNA sequencing:

After RNA extraction, mRNA was enriched by using Oligo dT beads from the KAPA mRNA Capture Kit (KK8581). Subsequent library preparation steps of fragmentation, adapter ligation and cDNA synthesis were done on the enriched mRNA using the KAPA RNA HyperPrep kit (KK8540). Truncated universal stub adapters were used for ligation, and indexed primers were used during PCR amplification to complete the adapters and to enrich the libraries for adapter-ligated fragments. Samples were checked for quality on an AATI (now Agilent) Fragment Analyzer. Samples were then transferred to the Vincent J. Coates Genomics Sequencing Laboratory (GSL), a QB3-Berkeley Core Research Facility at UC Berkeley, where Illumina sequencing library molarity was measured with quantitative PCR with the Kapa Biosystems Illumina Quant qPCR Kits on a BioRad CFX Connect thermal cycler. Libraries were then pooled evenly by molarity and sequenced on an Illumina NovaSeq6000 150PE S4 flowcell, generating 25M read pairs per sample. Raw sequencing data was converted into fastq format, sample specific files using the Illumina bcl2fastq2 software on the sequencing centers local linux server. For data analysis, kallisto, a program for quantifying abundances of transcripts from RNA-Seq data was used. Release 94 of the human reference transcriptome GRCh38 was downloaded from ENSEMBL on 7/20/2019. Relative abundances (reported as transcripts per million TPM values[84] and estimated counts (est_counts) of each transcript in each sample were estimated by alignment free comparison of k-mers between the pre-processed reads and the transcriptome using KALLISTO version 0.43.0[85]. Further analysis was restricted to transcripts with TPM >= 10 in at least one sample. Differentially expressed genes were identified by comparing replicate means for contrasts of interest using LIMMA version 3.30.8[86,87]. Genes were considered significantly differentially expressed if they were statistically significant (at 5% FDR) with an effect size of at least 2x (absolute log2 fold change >= 1) for a given contrast. LIMMA implements a two-sided moderated t-test with empirical Bayesian shrinkage. Principal components analysis (PCA)[88] was carried out on the matrix of sample vs. transcript log (TPMs) by mean centering the values for each gene and extracting principal components by singular value decomposition as implemented in Numpy 1.12.1[89]. Gene set enrichment analyses on the ranked list of genes was performed as previously described[33]. The RNA-seq datasets have been deposited in the GenBank database under the accession code GSE205648.

Indirect immunofluorescence and confocal microscopy:

Indirect immunofluorescence (IF) was performed as follows: cells grown on coverslips were washed in phosphate-buffered saline (PBS) and fixed in freshly prepared PBS

supplemented with 4% paraformaldehyde (Electron Microscopy Sciences, Hatfield, USA) for 30 min at room temperature (RT). Cells were permeabilized and blocked in blocking buffer (0.05% saponin in 0.5% BSA) for 30 min at room temperature. Primary antibodies were incubated for 1 hour at RT or overnight at 4°C in blocking buffer. Cells were subsequently labelled with appropriate Alexa 488/568- tagged fluorescent-conjugated secondary antibodies. Images were acquired using an inverted Nikon Eclipse Ti-E spinning disk confocal microscope equipped with a Prime 95B 25mm CMOS camera (Photometrics) camera. Identical settings for each channel were maintained throughout single experiments. For figure presentation only, the images were channel-separated, and each channel was merged after correcting for contrast using Image-J (NIH) or Adobe Photoshop CS3 (Adobe Systems).

Gene block synthesis and cloning of *ATF3* 5'-UTR:

Gene blocks were custom synthesized by Integrated DNA Technologies, Coralville, IA, USA based on the sequence of the 5'UTR and CDS of *ATF3* deposited into the GenBank database of NCBI (Accession number: NM_001674.3). The custom sequences were optimized to allow for manufacture of the gene block and share ~95% identity with the sequence deposited to GenBank (see Supplementary Table 7 for sequence information). The 5'-UTR of *ATF3* mRNA contains a putative translation start site and encodes an upstream open reading frame (uORF) that is 288 base pairs (bp) in length, begins at an AUG codon and includes the first 95 bp of exon 2 of the main *ATF3* CDS. A 399 bp optimized sequence of *ATF3* mRNA that encompassed these elements was synthesized and included the AUG start codon of the uORF but excluded the last 3 bp of the uORF that codes for an in-frame stop codon. A separate gene block where the AUG start codon in the uORF was altered to AGG was also synthesized. These gene blocks were subcloned by restriction free digestion into the pXG237 plasmid downstream of a cytomegalovirus (CMV) promoter and upstream of a fluorescent reporter mApple gene by replacing the uORF1 and uORF2 sequences of *ATF4* with the 5'-UTR sequences of *ATF3*. Comparative secondary structure prediction analyses using the RNAstructure web server[90] indicated that the custom gene block sequence and the GenBank sequence had similar free energies (-151) and no pseudo-knotted pairs.

Quantitative flow cytometry:

Cells were transfected with the 5'UTR *ATF3* reporter construct or the ATF4 translation reporter construct and were treated with ethanol (control) or ANS or transfected with pcDNA-FLAG (control) or FLAG-SidI for 16 hours. The cells were then trypsinized, washed with PBS and resuspended in ice-cold FACS buffer (sterile 1% BSA in PBS). The median intensity of mApple expression in 10,000 cells per replicate per treatment was determined by flow cytometry using a CytoFLEX benchtop flow cytometer from Beckman Coulter. The gating strategy and quantification of median intensities was performed according to previously published methods for the ATF4 translation reporter[91].

CRISPR-Cas9 mediated knockout of ATF3:

Ribonucleoprotein complexes containing 3.9 picomoles of ATF3 sgRNA guides and 3 picomoles of purified recombinant Cas9 protein (Synthego) were transfected into HEK293T

cells using Lipofectamine CRISPRmax (Invitrogen). 72 hours post transfection, cells were trypsinized and single cell dilutions were plated into 2 × 96 well plates (~1 cell/well) and allowed to grow in complete media for 7 days to facilitate clonal expansion. Viable clones were then trypsinized and seeded into replica 24 well plates and allowed to grow. A primary screen for CRISPR-Cas9 knockout efficiency was performed by lysing the clonal cell populations and subjecting the lysates to SDS-PAGE and immunoblotting with antibodies against ATF3. Clonal populations positive for the loss of ATF3 protein were expanded and their genomic DNA was isolated. Genotyping of clones was performed by PCR-amplifying exon 2 of the *ATF3* gene using the primers F: tggccacatttgcacataggcaca and R: acccagcaaccccatccctacc. The amplicons were sequenced and analyzed using Synthego's Inference of CRISPR Edits (ICE) tool. The ATF3 knockout HEK293T cell line clone D10 presented with indels in exon 2 of the *ATF3* gene and a complete loss of ATF3 protein as determined by immunoblotting with antibodies against ATF3.

Measurement of cell viability:

After indicated treatments, media was aspirated, and the cells were carefully scraped and diluted in fresh media. Media containing cells was then mixed in a 1:1 (v/v) ratio with 0.4% trypan blue, a dye that only stains non-viable cells with compromised membranes. 10μL of this mixture was mounted onto Countess cell counting chambers (Invitrogen) and the number of viable cells was determined by automatic counting using a Cell Countess FL II machine programmed with a plugin to highlight stained (non-viable) and unstained (viable) cells. The percentage of viable cells was calculated by normalizing total viable cell numbers to the counts obtained under control conditions.

Cell free transcription and translation in *E.coli* S30 extracts:

For each treatment condition, 1μg of luciferase DNA (pBEST*luc* Promega L485A) was transcribed and translated for 60 minutes at 37°C in reaction mixtures containing *E.coli* S30 extract (7.5μL), amino acid mixture without leucine (10μM), amino acid mixture without methionine (10μM) and *E.coli* S30 premix. 100μM of GDP-mannose was added to the reaction mixtures when indicated. After incubation, the samples were mixed in a 1:1 (v/v) ratio with luciferase assay reagent (Promega) in a 96-well white opaque plate and left at room temperature for 2 minutes. Luminescence readings were then obtained on a BioTek Cytation Imaging reader. The translation efficiency for each condition was calculated as a percentage of the raw luminescence values obtained when reaction mixtures were untreated.

Inferred kinase activity prediction from phosphoproteomics datasets:

Phosphoproteomics datasets generated by Noack *et al.*[43-preprint] were utilized for calculating kinase activity scores. To detect phosphorylation sites on host proteins during *L.p.* infections, HEK293 FcγR were infected for 1 hour with the *L.p.* WT strain or the *ΔdotA* strain at a MOI = 100. After infection, cells were washed with ice-cold PBS, scraped, and pelleted by centrifugation at 1500 rpm for 5 minutes at 4°C. Cell pellets were then lysed by probe sonication in three pulses of 20% amplitude for 15 seconds on ice in lysis buffer [8M urea, 150 mM NaCl, 100 mM ammonium bicarbonate, pH = 8; protease inhibitor and phosphatase inhibitor cocktails]. In order to remove insoluble precipitates, lysates were centrifuged at 16,000 g at 4°C for 30 min. 6 mg of protein isolated from each infection

condition was reduced with 4 mM tris(2-carboxyethyl) phosphine for 30 min at room temperature and alkylated with 10 mM iodoacetamide for 30 min at room temperature in the dark. Remaining alkylated agent was quenched with 10 mM 1,4-dithiothreitol for 30 min at room temperature in the dark. The samples were diluted with three starting volumes of 100 mM ammonium bicarbonate, pH 8.0, to reduce the urea concentration to 2 M. Samples were incubated with 50 μg of sequencing grade modified trypsin (Promega) and incubated at room temperature with rotation for 18 hours. The sample pH was reduced to approximately 2.0 by the addition of 10% trifluoroacetic acid (TFA) to a final concentration of 0.3% trifluoroacetic acid. Insoluble material was removed by centrifugation at 16,000 g for 10 min. Peptides were desalted using SepPak C18 solid-phase extraction cartridges (Waters). The columns were activated with 1 ml of 80% acetonitrile (ACN), 0.1% TFA, and equilibrated 3 times with 1 ml of 0.1% TFA. Peptide samples were applied to the columns, and the columns were washed 3 times with 1 ml of 0.1% TFA. Peptides were eluted with 1.2 ml of 50% ACN, 0.25% formic acid. Phosphopeptides were enriched by immobilized metal affinity chromatography. In-house prepared iron nitriloacetic acid coupled beads (Fe-NTA resin) were loaded into pre-equilibrated silica C18 microspin columns. Dried peptide samples were resuspended in a solution of 200 μl 75% ACN and 0.15% TFA. Peptide samples were mixed twice with the Fe- NTA resin, allowing the peptides to incubate for 2 minutes between each mixing step. The resin was rinsed four times with 200 μl of 80% ACN, 0.1% TFA. In order to equilibrate the columns, 200 μl of 0.5% formic acid was applied twice to the resin and columns. Peptides were then eluted from the resin onto the C18 column by mixing and incubating the Fe-NTA resin with 200 μl of 500 mM potassium phosphate, pH = 7.0 for 2 minutes. Peptides bound to the C18 column were washed three times with 200 μl of 0.5% formic acid. The C18 columns were removed from the vacuum manifold and the bound peptides were eluted by centrifugation at 1000g with 75 μl of 50% ACN, 0.25% formic acid. Peptides were dried with a centrifugal adaptor and stored at − 20°C until analysis by liquid chromatography and mass spectrometry. Samples were separated by a reverse phase gradient over a nanoflow column (360 μm O.D. × 75 μm I.D.) packed with 25 cm of 1.8 μm Reprosil C18 particles and directly injected into an Orbitrap Fusion Lumos Tribrid Mass Spectrometer (Thermo). Total acquisition time was 100 minutes. Raw MS data were searched with MaxQuant against the human proteome (UniProt canonical protein sequences downloaded January 11, 2016.

Kinase activity scores were calculated based on $\log_2$fold change values of all detected phosphosites (12751 phosphosites from 3113 proteins) during WT *L.p.* infection in comparison with *ΔdotA* infection using the bioinformatic tool PhosFate (http://phosfate.com)[92]. Due to space constraints, please refer to the Supplementary Methods for a detailed protocol.

Bioinformatic mining of ATF3 ChIP-seq tracks:

The human hg38 build on the UCSC genome browser was mined. The gene tracks represent the NCBI Ref Seq with the exons for each gene highlighted. The histone H3 lysine 27 acetylation tracks contain information relevant to the regulation of transcription from the ENCODE Project[93,94]. The Layered H3K27Ac tracks show where modification of histone proteins is suggestive of enhancer and, to a lesser extent, other regulatory activity. The

actual enhancers are typically just a small portion of the area marked by these histone modifications. These tracks are a cumulative representation of data collected from 7 different cell lines (GM12878, H1-hESC, HSMM, HUVEC, K562, NHEK and NHLF) and use a transparent overlay method of displaying data from a number of cell lines in the same vertical space. Each of the cell lines in this track is associated with a particular colour. The transcription factor ChIP-seq peaks for ATF3 were mined from ENCODE 3 and were generated by the ENCODE Transcription Factor ChIP-seq Processing Pipeline. Methods documentation and full metadata for each track can be found at the ENCODE project portal, using the ENCODE file accession (K562 = ENCFF937OKC; A549 = ENCFF851UTY; HepG2 = ENCFF137OEY; Liver cells = ENCFF146URA). The display for this track shows site location with the point-source of the peak marked with a red coloured vertical bar and the level of enrichment at the site indicated by the darkness of the item. The score values were computed at UCSC based on signal values assigned by the ENCODE pipeline. The input signal values were multiplied by a normalization factor calculated as the ratio of the maximum score value (1000) to the signal value at 1 standard deviation from the mean, with values exceeding 1000 capped at 1000.

Data Reproducibility and Statistical Analysis:

The number of replicates and statistical parameters for each experiment are listed in the corresponding figure legends. Unless specified otherwise, p-values were calculated with a two-tailed unpaired students t-test between respective control and test groups. No statistical methods were used to pre-determine sample sizes. Our sample sizes are similar to those reported in previous publications[6,27,67,68]. Data distribution was assumed to be normal, but this was not formally tested. Experimental design and data collection was randomized. For each experiment with multiple conditions, cultured cells or translation extracts were from the same source and allocated at random in culture dishes or test-tubes. The independent variable was controlled by direct manipulation. All other sources of extraneous variability were controlled by randomization or chance. As a collaborative study, each investigator was blinded from experiments, data collection, and analyses conducted by every other investigator. Data collection and analysis by an individual investigator was however not performed blind to the conditions of the experiments. For the densitometric analysis of western blots, protein bands on membranes were captured on a BioRad Chemidoc Touch apparatus. The exposure times were varied to obtain appropriate signal intensities of the protein bands. The intensities of each of the bands were quantitated using the Image-J gel analysis tool.

Extended Data

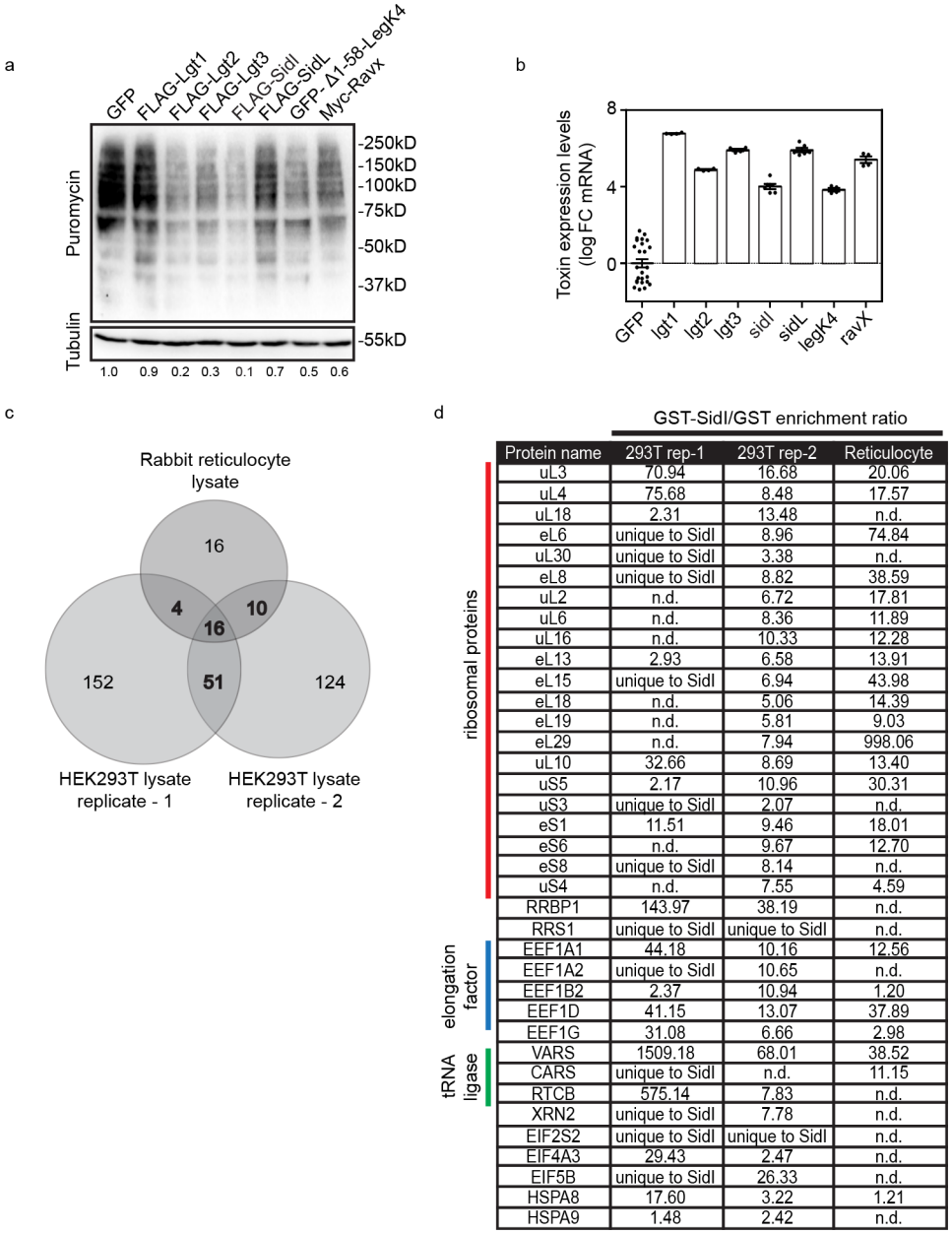

	Protein name	293T rep-1	293T rep-2	Reticulocyte
ribosomal proteins	uL3	70.94	16.68	20.06
	uL4	75.68	8.48	17.57
	uL18	2.31	13.48	n.d.
	eL6	unique to SidI	8.96	74.84
	uL30	unique to SidI	3.38	n.d.
	eL8	unique to SidI	8.82	38.59
	uL2	n.d.	6.72	17.81
	uL6	n.d.	8.36	11.89
	uL16	n.d.	10.33	12.28
	eL13	2.93	6.58	13.91
	eL15	unique to SidI	6.94	43.98
	eL18	n.d.	5.06	14.39
	eL19	n.d.	5.81	9.03
	eL29	n.d.	7.94	998.06
	uL10	32.66	8.69	13.40
	uS5	2.17	10.96	30.31
	uS3	unique to SidI	2.07	n.d.
	eS1	11.51	9.46	18.01
	eS6	n.d.	9.67	12.70
	eS8	unique to SidI	8.14	n.d.
	uS4	n.d.	7.55	4.59
	RRBP1	143.97	38.19	n.d.
	RRS1	unique to SidI	unique to SidI	n.d.
elongation factor	EEF1A1	44.18	10.16	12.56
	EEF1A2	unique to SidI	10.65	n.d.
	EEF1B2	2.37	10.94	1.20
	EEF1D	41.15	13.07	37.89
	EEF1G	31.08	6.66	2.98
tRNA ligase	VARS	1509.18	68.01	38.52
	CARS	unique to SidI	n.d.	11.15
	RTCB	575.14	7.83	n.d.
	XRN2	unique to SidI	7.78	n.d.
	EIF2S2	unique to SidI	unique to SidI	n.d.
	EIF4A3	29.43	2.47	n.d.
	EIF5B	unique to SidI	26.33	n.d.
	HSPA8	17.60	3.22	1.21
	HSPA9	1.48	2.42	n.d.

Extended Data Figure 1. (a-b) Analysis of protein synthesis rates in cells after heterologous expression of *L.p.* EITs.

(a) Cells expressing epitope tagged *L.p.* EITs subjected to puromycin pulse-chase analyses. Immunoblotting of lysates was performed using antibodies against puromycin and Tubulin. Data are representative of 2 independent experiments. Values below the immunoblots represent densitometric quantification of puromycylated peptides normalized to the amount of Tubulin in cells. (b) Expression levels of *L.p.* toxins were determined by qRT-PCR. Data represent mean ± standard error of the mean. n = independent replicates. *GFP* (n = 25); *lgt1*, *lgt2*, *lgt3*, *legK4* and *ravX* (n = 4); *sidI* and *sidL* (n = 6). Data were normalized to

the average Ct values of the reference gene ribosomal protein S29 (*RPS29*). **(c-d) Mass spectrometry analyses of SidI interacting partners highlights the translation machinery as targets of SidI.** (c) Venn diagram depicting the common interacting partners enriched in GST-SidI pulldown eluates from HEK293T cell lysates (n = 2) and rabbit reticulocyte lysates (n = 1). n = independent replicates. (d) List of translation machinery components selectively enriched by GST-SidI. GST-SidI enrichment is calculated as a ratio of the peptide intensities observed in GST-SidI pulldown eluates over GST pulldown eluates or marked as peptide intensities uniquely measured only in GST-SidI pulldown eluates. n.d. – not detected.

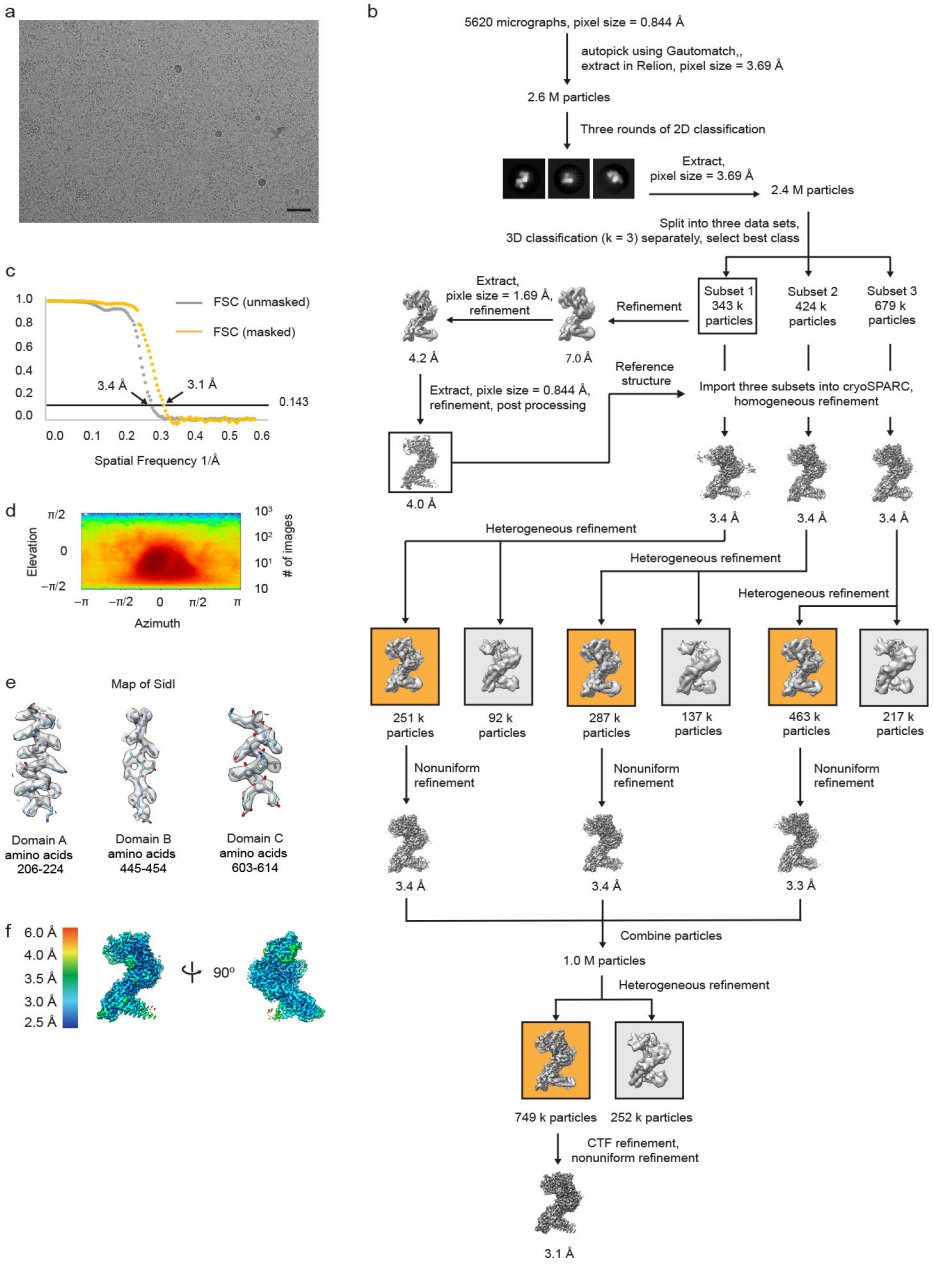

Extended Data Figure 2. Cryo-EM workflow and characterization of SidI structure.

(a) Representative micrograph (from n = 5620 micrograph images) showing the quality of data used for the final reconstruction of the SidI structure. Scale bar = 200 Å. (b) Data processing scheme of the SidI structure. (c) Fourier shell correlation (FSC) plots of the 3D reconstructions of SidI unmasked (grey), masked (orange). (d) Orientation angle distribution of the SidI reconstruction. (e) Electron microscopy maps of different regions of the SidI structure showing the quality of the data and the fit of the model. (f) Local resolution map of the SidI structure.

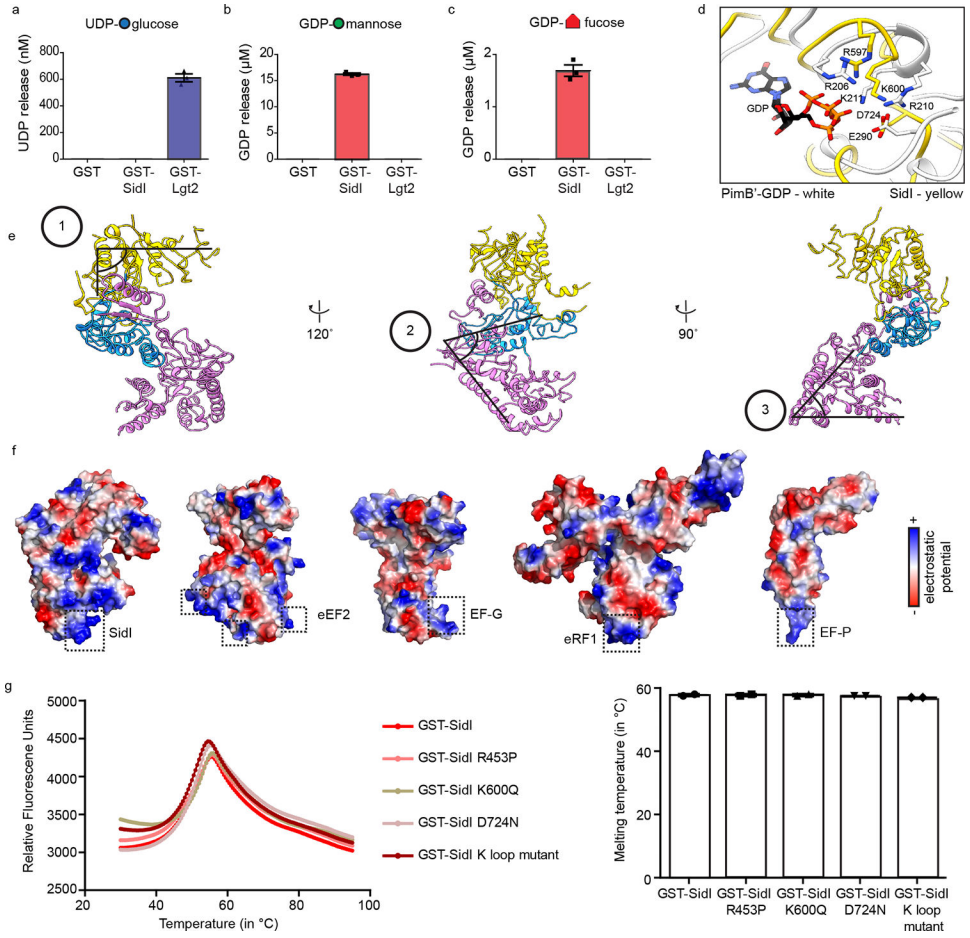

Extended Data Figure 3. Biochemical and biophysical characterization of SidI.

(a – c) GDP hydrolysis assay with 1μM of GST, GST-SidI and GST-Lgt2. 50μM of nucleotide-sugars were provided as precursors. Graphs depict amount of nucleotide release (Data represent mean ± standard error of the mean; n = 3 replicates per treatment condition). (d) Overlay of SidI (gold) and GDP-PimB' (light grey) showing the structural similarity between the enzymatic pockets and the conserved amino acids. (e) Different views of the SidI structure showing the three distinct kinks. (f) Surface charge distribution on the tRNA mimicry domains of SidI, eEF2, EF-G, eRF1 and EF-P. Box highlights the regions in eEF2, EF-G, eRF1 and EF-P that contact the ribosome. (g) Melting curve analyses of GST-SidI and GST-SidI mutants (n = 2 independent replicates).

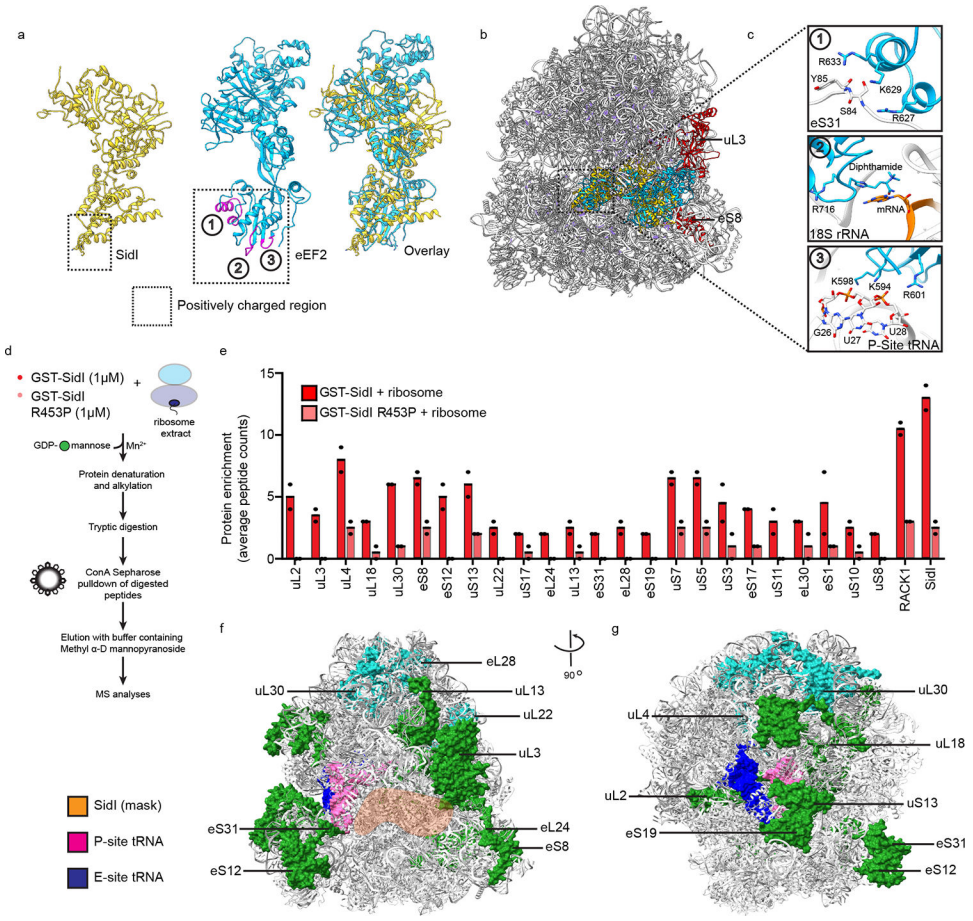

Extended Data Figure 4. Comparative structural, and functional enzymatic analyses of SidI reveals a potential mode of ribosome binding.

(a) Overlay of eEF2 and SidI structures showing their similarity in size and shape. The positively charged loops are boxed in black boxes. (b) Structure of SidI overlayed to the structure of eEF2 in the eEF2-bound ribosome structure (PDB ID: 6GZ5). (c) Zoomed-in view of the eEF2-ribosome complex showing the positively charge regions on eEF2 making contacts with (1) eS31; (2) 18S rRNA and (3) tRNA at the P-site. (d-e) Mass spectrometric analyses of Concanavalin-A enriched proteins after *in vitro* mannosylation reactions with 1μM of GST-SidI or GST-SidI R453P co-incubated with ribosomes (240nM) and GDP-mannose (50μM). Graphs depict average peptide counts of ribosomal proteins and SidI (n = 2 independent replicates). (f-g) Concanavalin-A enriched ribosomal proteins at/near the A-site/P-site and peptide exit tunnel of the ribosome (PDB ID: 6GZ5) are highlighted in green and blue respectively.

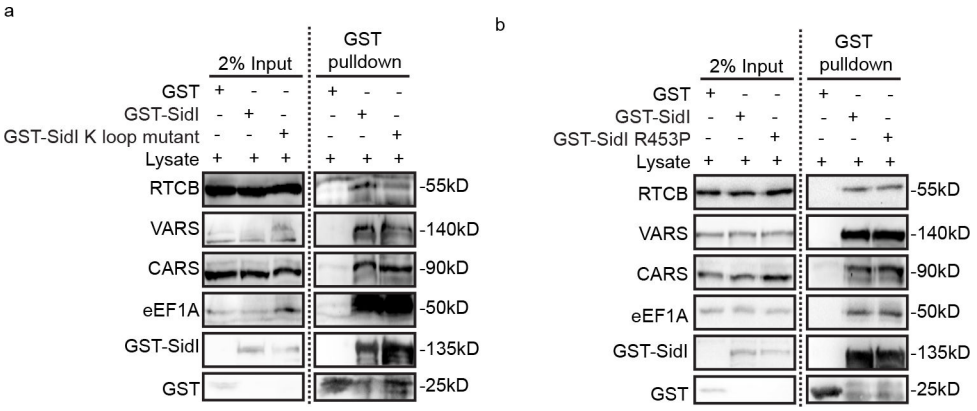

Extended Data Figure 5. SidI mutants precipitate eEF1A and tRNA ligases from HEK293T lysates.

Enrichment of interaction partners from HEK293T lysates with GST, GST-SidI, (a) GST-SidI K-rich loop mutant or (b) GST-SidI R453P pulldowns. Immunoblotting was performed using antibodies against RTCB, VARS, CARS, eEF1A and GST. Data are representative of 2 independent experiments.

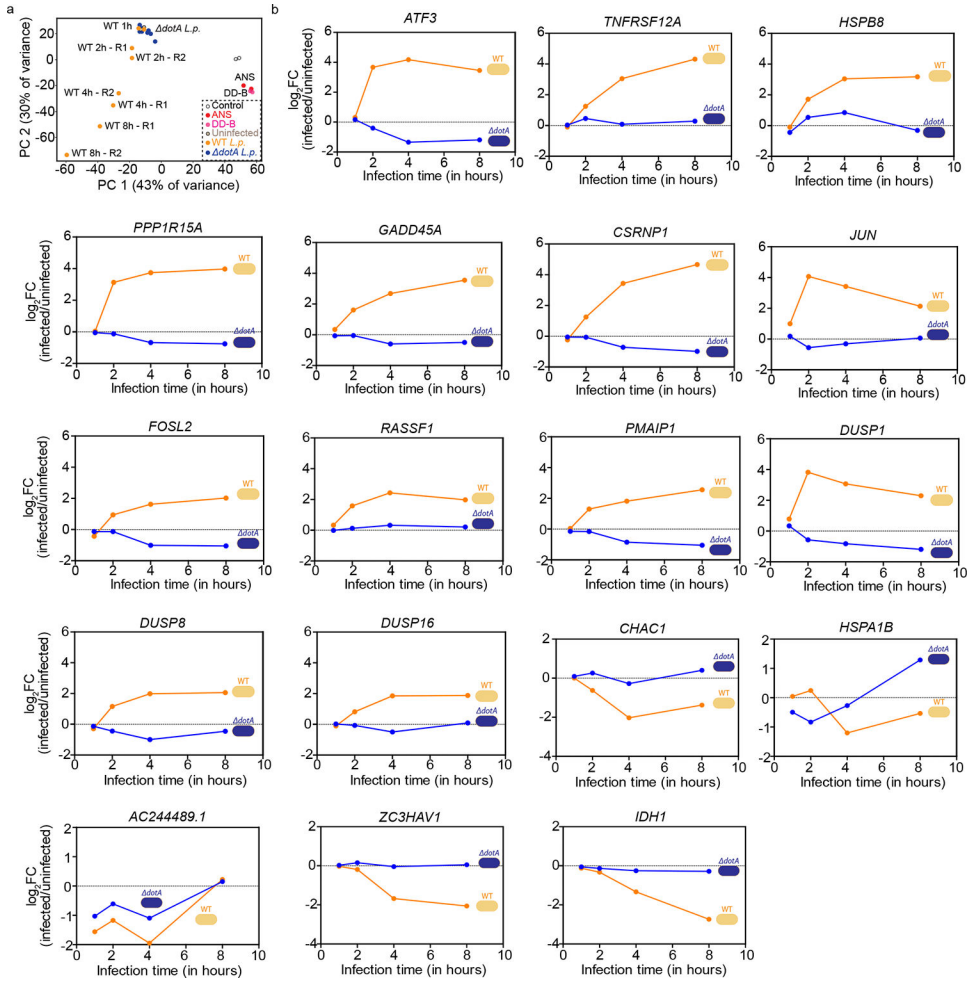

Extended Data Figure 6. Analyses of RNA-seq datasets reveals a dynamic induction of stress transcripts during *L.p.* infection in an effector dependent manner.

(a) Principal component analyses on all differentially expressed genes in HEK293 FcγR cells infected with WT and *ΔdotA L.p.* for 1 hour, 2 hours, 4 hours, and 8 hours and in HEK293T cells treated with ANS (0.1μM) and DD-B (0.1μM) for 4 hours. Coloured circles depict replicates. (b) Fold induction of upregulated and downregulated transcripts in common with transcripts induced by ribosome stalling insults. Expression levels of transcripts are after WT and *ΔdotA L.p.* infections normalized to uninfected controls. n = independent 2 replicates per time point.

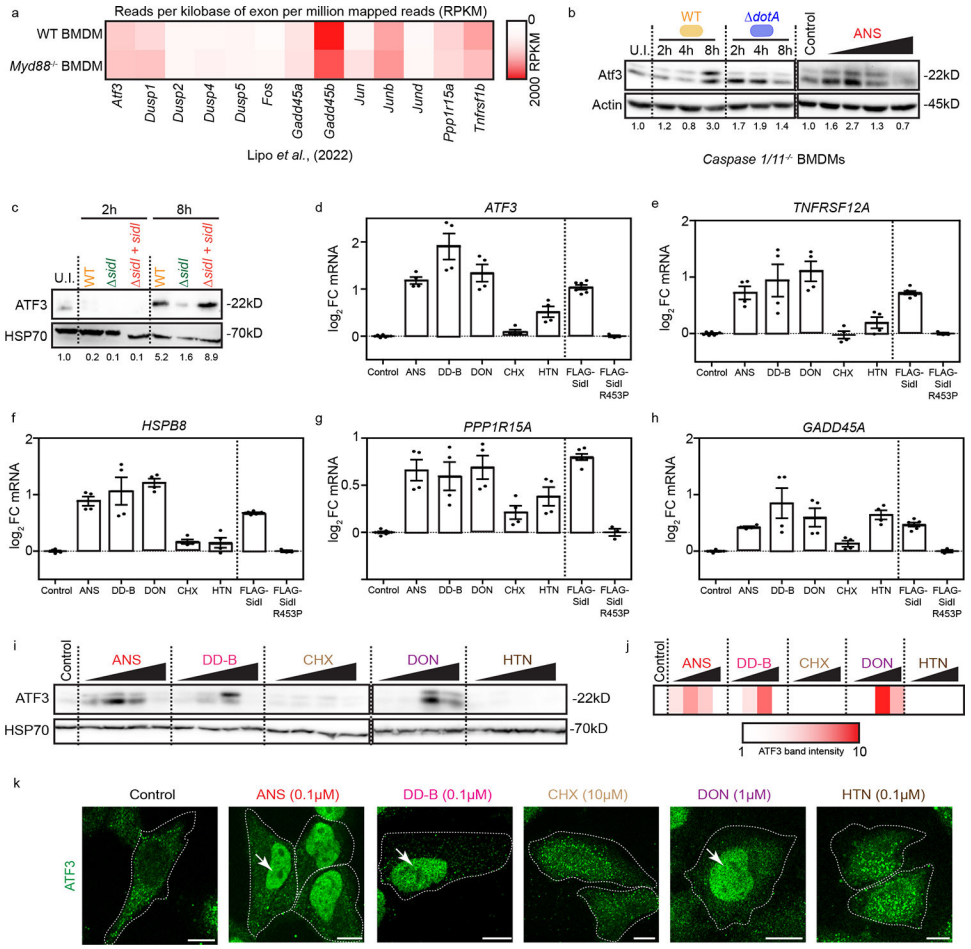

Extended Data Figure 7. Characterization of stress transcript induction and ATF3 accumulation by *L.p.* and inhibitors of ribosome function.

(a) Heat map of absolute stress transcript abundances (RPKM values) from *L.p.* infected macrophages extracted from RNA-seq datasets in Lipo *et al.*[32]. (b-c) Immunoblotting of ATF3 in lysates from (b) *Casp1/Casp11*$^{-/-}$ primary BMDM cells infected with WT or *ΔdotA L.p.* (MOI = 10) or treated with ANS (0.01μM, 0.1μM, 1μM, 10μM) and (c) HEK293 FcγR cells infected with indicated *L.p.* strains. Values below immunoblots depict densitometric quantification of ATF3 band intensities normalized to controls. Data are representative of 2 independent experiments. Gels were processed in parallel. (d-h) Fold induction of *ATF3*, *TNFRSF12A*, *HSPB8*, *PPP1R15A* and *GADD45A* mRNA measured by

qRT-PCR in HEK293T cells treated with vehicle control (n = 6), ANS 0.1μM (n = 4), DD-B 0.1μM (n = 4), DON 1μM (n = 4), CHX 0.1μM (n = 4) or HTN 0.1μM (n = 4) for 4 hours or expressing FLAG-SidI (n = 6) or FLAG-SidI R453P (n = 3) (Data represent mean ± standard error of the mean for n = independent replicates). Transcript expression values were normalized internally to the reference gene *RPS29* and expressed as $\log_2$fold change over the levels in controls. (i) Immunoblotting of ATF3 in lysates from HEK293T cells treated with ANS (0.01μM, 0.1μM, 1μM, 10μM); DD-B (0.001μM, 0.01μM, 0.1μM, 1μM); CHX (0.01μM, 0.1μM, 1μM, 10μM); DON (0.01μM, 0.1μM, 1μM, 10μM); and HTN (0.01μM, 0.1μM, 1μM, 10μM) for 4 hours. Data are representative of 3 independent experiments. Gels were processed in parallel. (j) Heat map of ATF3 band intensities measured by densitometric analyses of blots in (i). (k) Indirect immunofluorescence of ATF3 in HeLa cells treated with ANS, DD-B, CHX, DON and HTN at the indicated concentrations. Scale bar = 10μM. Data are representative of 2 independent experiments. Nuclear region is marked by arrows.

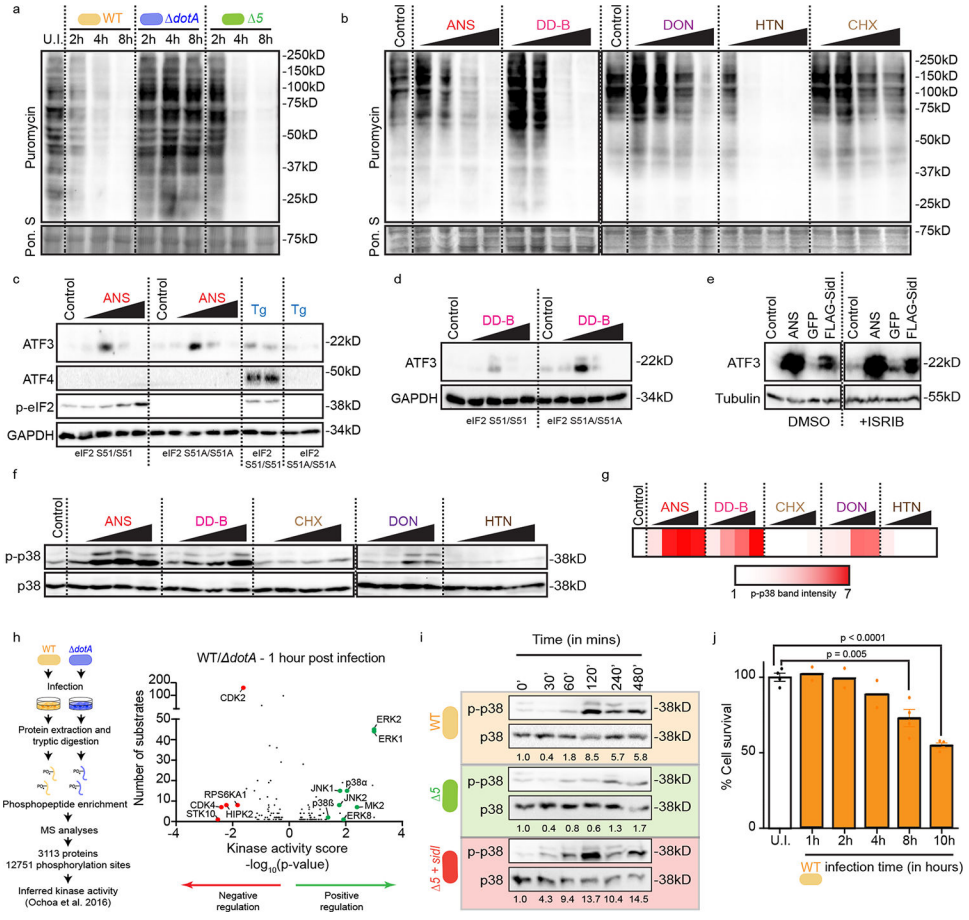

Extended Data Figure 8. Characterization of translation rates, stress signaling and cell viability during *L.p.* infections.

(a) Immunoblotting of lysates from cells infected with WT, *ΔdotA* and *Δ5 L.p.* was performed using antibodies against puromycin. Ponceau S staining of membranes serves as a loading control. Data are representative of 2 independent experiments. (b) Immunoblotting of lysates from cells treated with ANS (0.01μM, 0.1μM, 1μM, 10μM); DD-B (0.001μM,

0.01μM, 0.1μM, 1μM); CHX (0.01μM, 0.1μM, 1μM, 10μM); DON (0.01μM, 0.1μM, 1μM, 10μM); and HTN (0.01μM, 0.1μM, 1μM, 10μM) for 4 hours was performed using antibodies against puromycin. Ponceau S staining of membranes serves as a loading control. Gels were processed in parallel. Data are representative of 2 independent experiments. (c) Immunoblotting of ATF3, ATF4, phospho-eIF2 and GAPDH in lysates from WT or eIF2 $S51A^{+/+}$ mouse embryonic fibroblast cells treated with ANS (0.01μM, 0.1μM, 1μM and 10μM) or thapsigargin (Tg, 1μM) for 4 hours. Data are representative of 2 independent experiments. (d-e) Immunoblotting of ATF3 in lysates from (d) WT or eIF2 $S51A^{+/+}$ mouse embryonic fibroblast cells treated with DD-B (0.001μM, 0.01μM, 0.1μM and 1μM) for 4 hours; and (e) HEK293T cells treated with ANS (0.1μM) or transfected with FLAG-SidI in the absence or presence of ISRIB (200nM). Data are representative of 2 independent experiments. (f) Immunoblotting of phospho-p38 and total p38 in lysates of HEK293T cells treated with ANS (0.01μM, 0.1μM, 1μM, 10μM); DD-B (0.001μM, 0.01μM, 0.1μM, 1μM); CHX (0.01μM, 0.1μM, 1μM, 10μM); DON (0.01μM, 0.1μM, 1μM, 10μM); and HTN (0.01μM, 0.1μM, 1μM, 10μM) for 4 hours. Data are representative of 2 independent experiments. Gels were processed in parallel. (g) Heat map of p-p38 band intensities measured by densitometric analyses of blots in (f). (h) Phosphoproteomics pipeline and inferred kinase activation in WT *L.p.* infected cells (MOI = 100) based on the analyses of phosphorylation sites on proteins. Kinases of the mitogen and stress activated protein kinase pathways are positively regulated and highlighted in green. (i) Immunoblotting of phospho-p38 and total p38 in lysates from HEK293 FcγR cells infected with WT, *Δ5*, and *Δ5+sidI L.p.* strains (MOI = 50). Values below immunoblots represent densitometric quantification of phospho-p38 levels normalized to total p38 levels. Data are representative of 2 independent experiments. (j) Cell viability measurements in HEK293 FcγR cells infected with WT *L.p.* (MOI = 50; U.I., 8h, 10h samples (n = 4), 1h, 2h, 4h samples (n = 2). n = independent replicates per time point. For samples with n ≥ 3 data represent mean ± standard error of the mean. p-values were calculated by students t-test.

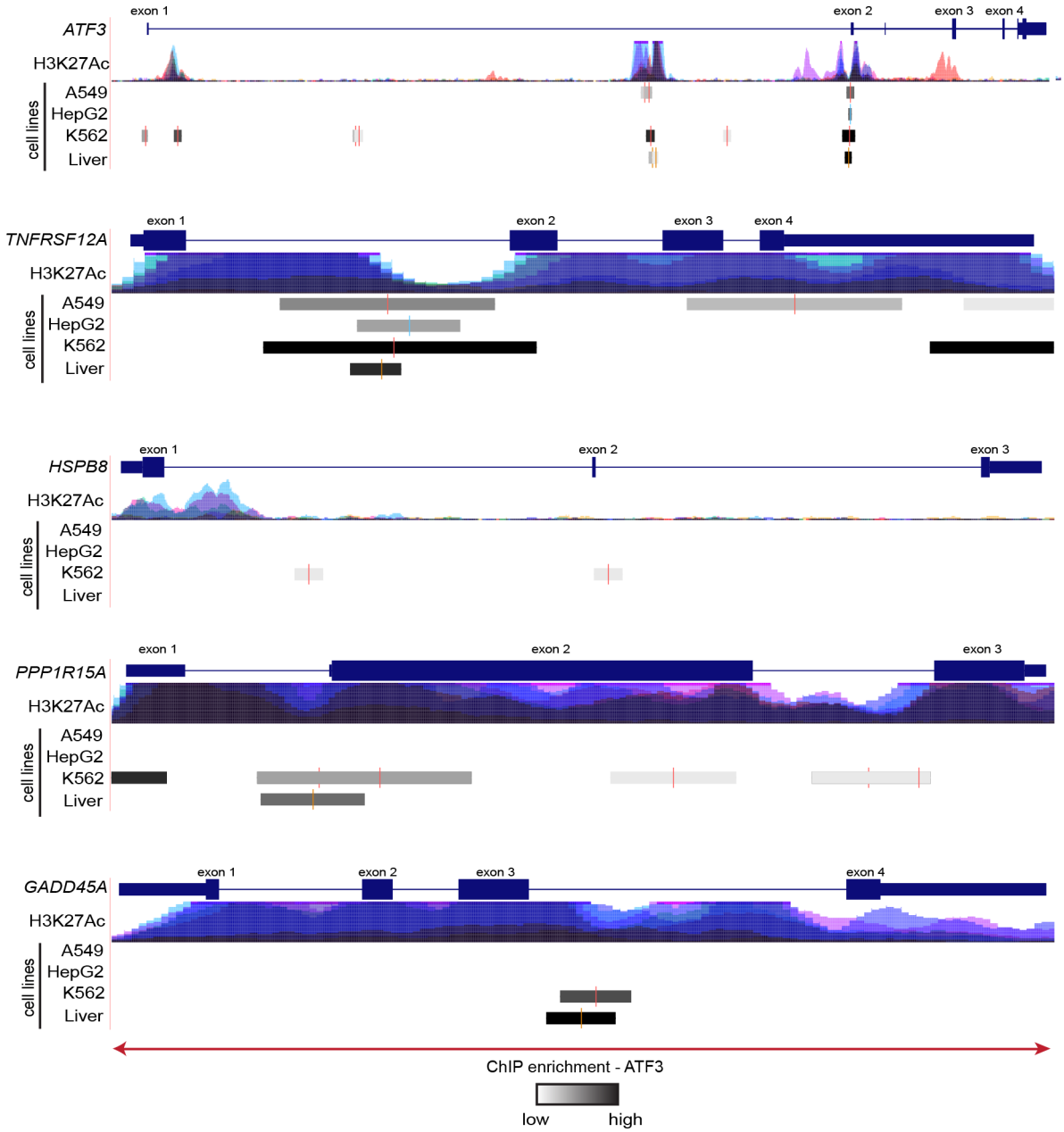

Extended Data Figure 9. ATF3 binds to genomic regions of stress inducible transcripts.

Mapping and enrichment of ATF3 binding zones on the *ATF3*, *TNFRSF12A*, *HSPB8*, *PPP1R15A* and *GADD45A* genes across four cell types. H3K27Ac tracks mark acetylation of lysine 27 of the H3 histone protein across 7 cell types (GM12878, H1-hESC, HSMM, HSMM, K562, NHEK and NHLF cells). Tracks of each cell type are marked with a different colour and displayed as a transparent overlay. The enrichment scores for ATF3 peaks were extracted from the ENCODE project datasets and visualized using UCSC genome browser (human hg38 assembly). The display for this track shows site location with the point-source of the peak marked with a coloured vertical bar and the level of enrichment at the site indicated by the darkness of the item. The enrichment values were computed based on signal values assigned by the ENCODE pipeline. The input signal values were multiplied by a

normalization factor calculated as the ratio of the maximum score value (1000) to the signal value at 1 standard deviation from the mean, with values exceeding 1000 capped at 1000.

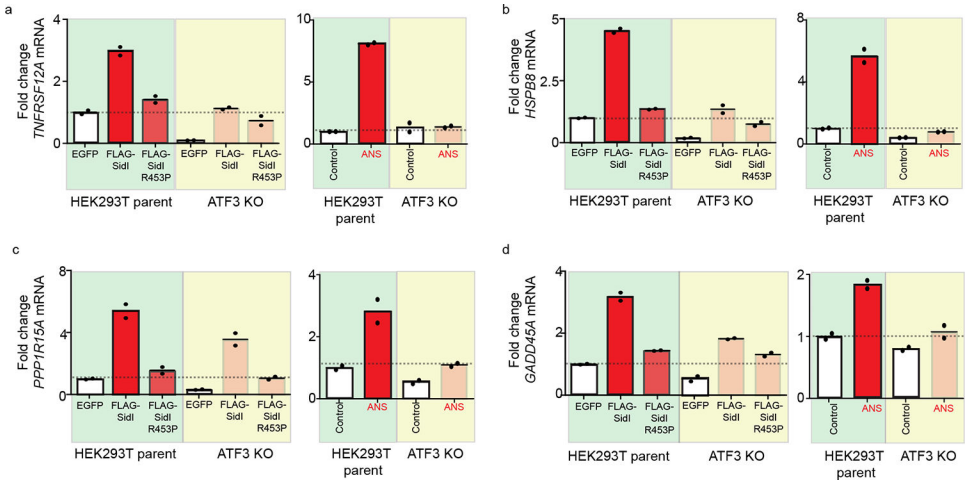

Extended Data Figure 10. ATF3 depletion attenuates stress transcript induction.

(a – d) Fold change induction of *TNFRSF12A*, *HSPB8*, *PPP1R15A* and *GADD45A* mRNA in parent and ATF3 KO HEK293T cells expressing GFP, FLAG-SidI or FLAG-SidI R453P or treated with ANS (0.1μM) measured by qRT-PCR (n = 2 independent replicates). Transcript expression values were normalized internally to the reference gene *RPS29* and expressed as fold change over the levels in GFP expressing cells.

Supplementary Material

Refer to Web version on PubMed Central for supplementary material.

Acknowledgements

We thank all members of the S.M. and P.W. labs for critical evaluation and discussions of the data. We thank Dr. Zhao-Qing Luo for his generous gift of isogenic Δ*sidI* and SidI complemented *L.p.* strains. We thank Srivats Venkatraman and Lorenzo Calviello from the Floor lab for helpful discussions. We thank Bassem Al-Sady and Eric Simental from the Al Sady lab for help with radioactivity experiments. We thank Jackie Yee from the Spitzer Lab for help with flow cytometry experiments. We thank Julia Noack, CJ Sarabia, and Brian Wang, for technical assistance with the project. L.W. acknowledges a fellowship from the Damon Runyon Cancer Research Foundation (DRG-2312-17). S.S. is supported by Helen Hay Whitney Postdoc fellowship and K99 (1K99GM143527-01A1) from NIGMS. N.J.K acknowledges financial support from the National Institutes of Health (U19 AI135990). A.L.B acknowledges financial support from the Dr. Miriam and Sheldon G. Adelson Medical Research Foundation. S.N.F. is a Pew Scholar in the Biomedical Sciences, supported by The Pew Charitable Trusts and acknowledges financial support from the National Institutes of Health (DP2GM132932). A.Si. acknowledges financial support from the National Institutes of Health (R01AI136735) and a gift fund from the Chan-Zuckerberg Biohub. P.W. acknowledges financial support from the National Institutes of Health (R01GM032384) and the Howard Hughes Medical Institute. S.M. acknowledges financial support from the National Institutes of Health (R01GM140440, R01GM144378), the Pew Charitable Trust (A129837), the Bowes Biomedical Investigator award, and a gift fund from the Chan-Zuckerberg Biohub. We thank the Vincent J. Coates Genomics Sequencing Laboratory at the California Institute for Quantitative Biosciences (QB3) for help with the RNA-seq experiments. We also thank the QB3 shared cluster for computational support.

Data Availability Statement

Key Resource information is available in Supplementary Table 9. Further information and requests for resources and reagents will be fulfilled by Shaeri Mukherjee

(shaeri.mukherjee@ucsf.edu). The authors declare that the data supporting the findings of this study are available within the article and its supplementary information files. The atomic models of BshA (PDB ID: 5D00), PimB' (PDB ID: 3OKA) and EEF2 bound to the ribosome (PDB ID:6GZ5) were downloaded from the Protein Data Bank (PDB). The atomic model of SidI has been deposited into PDB (PDB ID: 8JHU) and the EM map has been deposited into EMDB (EMDB ID: EMD-36294). Mass spectrometry data files for Supplementary Table 1 (raw and search results) have been deposited to the ProteomeXchange Consortium (http://proteomecentral.proteomexchange.org) via the PRIDE partner repository with dataset identifier PXD034240. Mass spectrometry data files for Supplementary Table 3 (raw and search results) have been deposited to the MassIVE repository with dataset identifier MSV000091992. The RNA-seq datasets have been deposited in the GenBank database under the accession code GSE205648. The nucleotide sequence of *ATF3* mRNA was downloaded from the NCBI GenBank database (NM_001674.3). ChIP-seq data were mined from the publicly available ENCODE 3 database and the tracks were generated by the ENCODE Transcription Factor ChIP-seq Processing Pipeline using UCSC Genome Browser. Methods documentation and full metadata for each track can be found at the ENCODE project portal, using the ENCODE file accession (K562 = ENCFF937OKC; A549 = ENCFF851UTY; HepG2 = ENCFF137OEY; Liver cells = ENCFF146URA).

References

1. Barry KC, Ingolia NT & Vance RE Global analysis of gene expression reveals mRNA superinduction is required for the inducible immune response to a bacterial pathogen. eLife 6, doi:10.7554/eLife.22707 (2017).
2. Belyi Y et al. Legionella pneumophila glucosyltransferase inhibits host elongation factor 1A. Proceedings of the National Academy of Sciences of the United States of America 103, 16953–16958, doi:10.1073/pnas.0601562103 (2006). [PubMed: 17068130]
3. Fontana MF et al. Secreted bacterial effectors that inhibit host protein synthesis are critical for induction of the innate immune response to virulent Legionella pneumophila. PLoS pathogens 7, e1001289, doi:10.1371/journal.ppat.1001289 (2011). [PubMed: 21390206]
4. McCusker KT, Braaten BA, Cho MW & Low DA Legionella pneumophila inhibits protein synthesis in Chinese hamster ovary cells. Infection and immunity 59, 240–246, doi:10.1128/iai.59.1.240-246.1991 (1991). [PubMed: 1987039]
5. Shen X et al. Targeting eEF1A by a Legionella pneumophila effector leads to inhibition of protein synthesis and induction of host stress response. Cellular microbiology 11, 911–926, doi:10.1111/j.1462-5822.2009.01301.x (2009). [PubMed: 19386084]
6. Moss SM et al. A Legionella pneumophila Kinase Phosphorylates the Hsp70 Chaperone Family to Inhibit Eukaryotic Protein Synthesis. Cell host & microbe 25, 454–462 e456, doi:10.1016/j.chom.2019.01.006 (2019). [PubMed: 30827827]
7. Belyi Y, Tabakova I, Stahl M & Aktories K Lgt: a family of cytotoxic glucosyltransferases produced by Legionella pneumophila. Journal of bacteriology 190, 3026–3035, doi:10.1128/JB.01798-07 (2008). [PubMed: 18281405]
8. Joseph AM et al. The Legionella pneumophila Metaeffector Lpg2505 (MesI) Regulates SidI-Mediated Translation Inhibition and Novel Glycosyl Hydrolase Activity. Infection and immunity 88, doi:10.1128/IAI.00853-19 (2020).
9. Guo Z, Stephenson R, Qiu J, Zheng S & Luo ZQ A Legionella effector modulates host cytoskeletal structure by inhibiting actin polymerization. Microbes and infection 16, 225–236, doi:10.1016/j.micinf.2013.11.007 (2014). [PubMed: 24286927]

10. Fontana MF, Shin S & Vance RE Activation of host mitogen-activated protein kinases by secreted Legionella pneumophila effectors that inhibit host protein translation. Infection and immunity 80, 3570–3575, doi:10.1128/IAI.00557-12 (2012). [PubMed: 22851749]
11. Joazeiro CAP Mechanisms and functions of ribosome-associated protein quality control. Nature reviews. Molecular cell biology 20, 368–383, doi:10.1038/s41580-019-0118-2 (2019). [PubMed: 30940912]
12. Wu CC, Peterson A, Zinshteyn B, Regot S & Green R Ribosome Collisions Trigger General Stress Responses to Regulate Cell Fate. Cell 182, 404–416 e414, doi:10.1016/j.cell.2020.06.006 (2020). [PubMed: 32610081]
13. Sinha NK et al. EDF1 coordinates cellular responses to ribosome collisions. eLife 9, doi:10.7554/eLife.58828 (2020).
14. Costa-Mattioli M & Walter P The integrated stress response: From mechanism to disease. Science 368, doi:10.1126/science.aat5314 (2020).
15. Iordanov MS et al. Ribotoxic stress response: activation of the stress-activated protein kinase JNK1 by inhibitors of the peptidyl transferase reaction and by sequence-specific RNA damage to the alpha-sarcin/ricin loop in the 28S rRNA. Molecular and cellular biology 17, 3373–3381, doi:10.1128/MCB.17.6.3373 (1997). [PubMed: 9154836]
16. Vind AC et al. ZAKalpha Recognizes Stalled Ribosomes through Partially Redundant Sensor Domains. Molecular cell 78, 700–713 e707, doi:10.1016/j.molcel.2020.03.021 (2020). [PubMed: 32289254]
17. Olsnes S, Refsnes K & Pihl A Mechanism of action of the toxic lectins abrin and ricin. Nature 249, 627–631, doi:10.1038/249627a0 (1974). [PubMed: 4857870]
18. Moremen KW & Haltiwanger RS Emerging structural insights into glycosyltransferase-mediated synthesis of glycans. Nature chemical biology 15, 853–864, doi:10.1038/s41589-019-0350-2 (2019). [PubMed: 31427814]
19. Batt SM et al. Acceptor substrate discrimination in phosphatidyl-myo-inositol mannoside synthesis: structural and mutational analysis of mannosyltransferase Corynebacterium glutamicum PimB'. The Journal of biological chemistry 285, 37741–37752, doi:10.1074/jbc.M110.165407 (2010). [PubMed: 20843801]
20. Lu W et al. Structural basis of the action of glucosyltransferase Lgt1 from Legionella pneumophila. Journal of molecular biology 396, 321–331, doi:10.1016/j.jmb.2009.11.044 (2010). [PubMed: 19941871]
21. Flis J et al. tRNA Translocation by the Eukaryotic 80S Ribosome and the Impact of GTP Hydrolysis. Cell reports 25, 2676–2688 e2677, doi:10.1016/j.celrep.2018.11.040 (2018). [PubMed: 30517857]
22. Song H et al. The crystal structure of human eukaryotic release factor eRF1--mechanism of stop codon recognition and peptidyl-tRNA hydrolysis. Cell 100, 311–321, doi:10.1016/s0092-8674(00)80667-4 (2000). [PubMed: 10676813]
23. Nissen P et al. Crystal structure of the ternary complex of Phe-tRNAPhe, EF-Tu, and a GTP analog. Science 270, 1464–1472, doi:10.1126/science.270.5241.1464 (1995). [PubMed: 7491491]
24. Blaha G, Stanley RE & Steitz TA Formation of the first peptide bond: the structure of EF-P bound to the 70S ribosome. Science 325, 966–970, doi:10.1126/science.1175800 (2009). [PubMed: 19696344]
25. Jank T et al. Domain organization of Legionella effector SetA. Cellular microbiology 14, 852–868, doi:10.1111/j.1462-5822.2012.01761.x (2012). [PubMed: 22288428]
26. Levanova N et al. The Legionella effector LtpM is a new type of phosphoinositide-activated glucosyltransferase. The Journal of biological chemistry 294, 2862–2879, doi:10.1074/jbc.RA118.005952 (2019). [PubMed: 30573678]
27. Mukherjee S et al. Modulation of Rab GTPase function by a protein phosphocholine transferase. Nature 477, 103–106, doi:10.1038/nature10335 (2011). [PubMed: 21822290]
28. Juszkiewicz S et al. ZNF598 Is a Quality Control Sensor of Collided Ribosomes. Molecular cell 72, 469–481 e467, doi:10.1016/j.molcel.2018.08.037 (2018). [PubMed: 30293783]

29. Ishimura R, Nagy G, Dotu I, Chuang JH & Ackerman SL Activation of GCN2 kinase by ribosome stalling links translation elongation with translation initiation. eLife 5, doi:10.7554/eLife.14295 (2016).
30. Vogel JP, Andrews HL, Wong SK & Isberg RR Conjugative transfer by the virulence system of Legionella pneumophila. Science 279, 873–876, doi:10.1126/science.279.5352.873 (1998). [PubMed: 9452389]
31. Roy CR, Berger KH & Isberg RR Legionella pneumophila DotA protein is required for early phagosome trafficking decisions that occur within minutes of bacterial uptake. Molecular microbiology 28, 663–674, doi:10.1046/j.1365-2958.1998.00841.x (1998). [PubMed: 9632267]
32. Shao S et al. Decoding Mammalian Ribosome-mRNA States by Translational GTPase Complexes. Cell 167, 1229–1240 e1215, doi:10.1016/j.cell.2016.10.046 (2016). [PubMed: 27863242]
33. Subramanian A et al. Gene set enrichment analysis: a knowledge-based approach for interpreting genome-wide expression profiles. Proceedings of the National Academy of Sciences of the United States of America 102, 15545–15550, doi:10.1073/pnas.0506580102 (2005). [PubMed: 16199517]
34. Lipo E et al. 5' Untranslated mRNA Regions Allow Bypass of Host Cell Translation Inhibition by Legionella pneumophila. Infection and immunity 90, e0017922, doi:10.1128/iai.00179-22 (2022). [PubMed: 36321832]
35. Garreau de Loubresse N et al. Structural basis for the inhibition of the eukaryotic ribosome. Nature 513, 517–522, doi:10.1038/nature13737 (2014). [PubMed: 25209664]
36. Eferl R & Wagner EF AP-1: a double-edged sword in tumorigenesis. Nature reviews. Cancer 3, 859–868, doi:10.1038/nrc1209 (2003). [PubMed: 14668816]
37. Fonseca GJ et al. Diverse motif ensembles specify non-redundant DNA binding activities of AP-1 family members in macrophages. Nature communications 10, 414, doi:10.1038/s41467-018-08236-0 (2019).
38. Hai T, Wolfgang CD, Marsee DK, Allen AE & Sivaprasad U ATF3 and stress responses. Gene expression 7, 321–335 (1999). [PubMed: 10440233]
39. Scheuner D et al. Translational control is required for the unfolded protein response and in vivo glucose homeostasis. Molecular cell 7, 1165–1176, doi:10.1016/s1097-2765(01)00265-9 (2001). [PubMed: 11430820]
40. Harding HP, Zhang Y & Ron D Protein translation and folding are coupled by an endoplasmic-reticulum-resident kinase. Nature 397, 271–274, doi:10.1038/16729 (1999). [PubMed: 9930704]
41. Jiang HY et al. Activating transcription factor 3 is integral to the eukaryotic initiation factor 2 kinase stress response. Molecular and cellular biology 24, 1365–1377, doi:10.1128/MCB.24.3.1365-1377.2004 (2004). [PubMed: 14729979]
42. Sidrauski C et al. Pharmacological brake-release of mRNA translation enhances cognitive memory. eLife 2, e00498, doi:10.7554/eLife.00498 (2013). [PubMed: 23741617]
43. Noack J et al. Dynamic proteomics profiling of Legionella pneumophila infection unveils modulation of the host mitochondrial stress response pathway. bioRxiv, 2020.2005.2019.105395, doi:10.1101/2020.05.19.105395 (2020).
44. Shin S et al. Type IV secretion-dependent activation of host MAP kinases induces an increased proinflammatory cytokine response to Legionella pneumophila. PLoS pathogens 4, e1000220, doi:10.1371/journal.ppat.1000220 (2008). [PubMed: 19043549]
45. Yang J et al. Design, Synthesis, and Structure-Activity Relationships of 1,2,3-Triazole Benzenesulfonamides as New Selective Leucine-Zipper and Sterile-alpha Motif Kinase (ZAK) Inhibitors. Journal of medicinal chemistry 63, 2114–2130, doi:10.1021/acs.jmedchem.9b00664 (2020). [PubMed: 31244114]
46. Pearlman E, Jiwa AH, Engleberg NC & Eisenstein BI Growth of Legionella pneumophila in a human macrophage-like (U937) cell line. Microbial pathogenesis 5, 87–95, doi:10.1016/0882-4010(88)90011-3 (1988). [PubMed: 3237054]
47. Marra A, Horwitz MA & Shuman HA The HL-60 model for the interaction of human macrophages with the Legionnaires' disease bacterium. Journal of immunology 144, 2738–2744 (1990).
48. Zink SD, Pedersen L, Cianciotto NP & Abu-Kwaik Y The Dot/Icm type IV secretion system of Legionella pneumophila is essential for the induction of apoptosis in human macrophages.

Infection and immunity 70, 1657–1663, doi:10.1128/IAI.70.3.1657-1663.2002 (2002). [PubMed: 11854262]

49. Lord JM, Roberts LM & Robertus JD Ricin: structure, mode of action, and some current applications. FASEB journal : official publication of the Federation of American Societies for Experimental Biology 8, 201–208 (1994). [PubMed: 8119491]
50. Shames SR et al. Multiple Legionella pneumophila effector virulence phenotypes revealed through high-throughput analysis of targeted mutant libraries. Proceedings of the National Academy of Sciences of the United States of America 114, E10446–E10454, doi:10.1073/pnas.1708553114 (2017). [PubMed: 29133401]
51. McCloskey A, Perri K, Chen T, Han A & Luo ZQ The metaeffector MesI regulates the activity of the Legionella effector SidI through direct protein-protein interactions. Microbes and infection 23, 104794, doi:10.1016/j.micinf.2021.104794 (2021). [PubMed: 33571674]
52. Mailliot J et al. Crystal Structures of the uL3 Mutant Ribosome: Illustration of the Importance of Ribosomal Proteins for Translation Efficiency. Journal of molecular biology 428, 2195–2202, doi:10.1016/j.jmb.2016.02.013 (2016). [PubMed: 26906928]
53. Meskauskas A, Russ JR & Dinman JD Structure/function analysis of yeast ribosomal protein L2. Nucleic acids research 36, 1826–1835, doi:10.1093/nar/gkn034 (2008). [PubMed: 18263608]
54. Diedrich G et al. Ribosomal protein L2 is involved in the association of the ribosomal subunits, tRNA binding to A and P sites and peptidyl transfer. The EMBO journal 19, 5241–5250, doi:10.1093/emboj/19.19.5241 (2000). [PubMed: 11013226]
55. Schulze H & Nierhaus KH Minimal set of ribosomal components for reconstitution of the peptidyltransferase activity. The EMBO journal 1, 609–613, doi:10.1002/j.1460-2075.1982.tb01216.x (1982). [PubMed: 6765232]
56. Lawrence MG et al. The extended loops of ribosomal proteins uL4 and uL22 of Escherichia coli contribute to ribosome assembly and protein translation. Nucleic acids research 44, 5798–5810, doi:10.1093/nar/gkw493 (2016). [PubMed: 27257065]
57. Gregory ST & Dahlberg AE Erythromycin resistance mutations in ribosomal proteins L22 and L4 perturb the higher order structure of 23 S ribosomal RNA. Journal of molecular biology 289, 827–834, doi:10.1006/jmbi.1999.2839 (1999). [PubMed: 10369764]
58. Zaman S, Fitzpatrick M, Lindahl L & Zengel J Novel mutations in ribosomal proteins L4 and L22 that confer erythromycin resistance in Escherichia coli. Molecular microbiology 66, 1039–1050, doi:10.1111/j.1365-2958.2007.05975.x (2007). [PubMed: 17956547]
59. Wong W et al. Mefloquine targets the Plasmodium falciparum 80S ribosome to inhibit protein synthesis. Nature microbiology 2, 17031, doi:10.1038/nmicrobiol.2017.31 (2017).
60. Mo P, Wang H, Lu H, Boyd DD & Yan C MDM2 mediates ubiquitination and degradation of activating transcription factor 3. The Journal of biological chemistry 285, 26908–26915, doi:10.1074/jbc.M110.132597 (2010). [PubMed: 20592017]
61. Vu TTM & Varshavsky A The ATF3 Transcription Factor Is a Short-Lived Substrate of the Arg/N-Degron Pathway. Biochemistry 59, 2796–2812, doi:10.1021/acs.biochem.0c00514 (2020). [PubMed: 32692156]
62. Losick VP & Isberg RR NF-kappaB translocation prevents host cell death after low-dose challenge by Legionella pneumophila. The Journal of experimental medicine 203, 2177–2189, doi:10.1084/jem.20060766 (2006). [PubMed: 16940169]
63. Farbrother P et al. Dictyostelium transcriptional host cell response upon infection with Legionella. Cellular microbiology 8, 438–456, doi:10.1111/j.1462-5822.2005.00633.x (2006). [PubMed: 16469056]
64. Li Z et al. The amoebal MAP kinase response to Legionella pneumophila is regulated by DupA. Cell host & microbe 6, 253–267, doi:10.1016/j.chom.2009.08.005 (2009). [PubMed: 19748467]
65. Case CL et al. Caspase-11 stimulates rapid flagellin-independent pyroptosis in response to Legionella pneumophila. Proceedings of the National Academy of Sciences of the United States of America 110, 1851–1856, doi:10.1073/pnas.1211521110 (2013). [PubMed: 23307811]
66. Sol A et al. Legionella pneumophila translocated translation inhibitors are required for bacterial-induced host cell cycle arrest. Proceedings of the National Academy of Sciences of the United States of America 116, 3221–3228, doi:10.1073/pnas.1820093116 (2019). [PubMed: 30718423]

67. Ibe NU, Subramanian A & Mukherjee S Non-canonical activation of the ER stress sensor ATF6 by Legionella pneumophila effectors. Life science alliance 4, doi:10.26508/lsa.202101247 (2021).

68. Treacy-Abarca S & Mukherjee S Legionella suppresses the host unfolded protein response via multiple mechanisms. Nature communications 6, 7887, doi:10.1038/ncomms8887 (2015).

69. Hubber A & Roy CR Modulation of host cell function by Legionella pneumophila type IV effectors. Annual review of cell and developmental biology 26, 261–283, doi:10.1146/annurev-cellbio-100109-104034 (2010).

70. Hempstead AD & Isberg RR Inhibition of host cell translation elongation by Legionella pneumophila blocks the host cell unfolded protein response. Proceedings of the National Academy of Sciences of the United States of America 112, E6790–6797, doi:10.1073/pnas.1508716112 (2015). [PubMed: 26598709]

71. De Leon JA et al. Positive and Negative Regulation of the Master Metabolic Regulator mTORC1 by Two Families of Legionella pneumophila Effectors. Cell reports 21, 2031–2038, doi:10.1016/j.celrep.2017.10.088 (2017). [PubMed: 29166595]

Methods only References

72. Isaac DT et al. Macrophage cell death and transcriptional response are actively triggered by the fungal virulence factor Cbp1 during H. capsulatum infection. Molecular microbiology 98, 910–929, doi:10.1111/mmi.13168 (2015). [PubMed: 26288377]

73. Zheng SQ et al. MotionCor2: anisotropic correction of beam-induced motion for improved cryo-electron microscopy. Nature methods 14, 331–332, doi:10.1038/nmeth.4193 (2017). [PubMed: 28250466]

74. Zhang K Gctf: Real-time CTF determination and correction. Journal of structural biology 193, 1–12, doi:10.1016/j.jsb.2015.11.003 (2016). [PubMed: 26592709]

75. Scheres SH RELION: implementation of a Bayesian approach to cryo-EM structure determination. Journal of structural biology 180, 519–530, doi:10.1016/j.jsb.2012.09.006 (2012). [PubMed: 23000701]

76. Punjani A, Rubinstein JL, Fleet DJ & Brubaker MA cryoSPARC: algorithms for rapid unsupervised cryo-EM structure determination. Nature methods 14, 290–296, doi:10.1038/nmeth.4169 (2017). [PubMed: 28165473]

77. Kallberg M, Margaryan G, Wang S, Ma J & Xu J RaptorX server: a resource for template-based protein structure modeling. Methods in molecular biology 1137, 17–27, doi:10.1007/978-1-4939-0366-5_2 (2014). [PubMed: 24573471]

78. Winchell KR et al. A Structural, Functional, and Computational Analysis of BshA, the First Enzyme in the Bacillithiol Biosynthesis Pathway. Biochemistry 55, 4654–4665, doi:10.1021/acs.biochem.6b00472 (2016). [PubMed: 27454321]

79. Emsley P, Lohkamp B, Scott WG & Cowtan K Features and development of Coot. Acta crystallographica. Section D, Biological crystallography 66, 486–501, doi:10.1107/S0907444910007493 (2010). [PubMed: 20383002]

80. Adams PD et al. PHENIX: a comprehensive Python-based system for macromolecular structure solution. Acta crystallographica. Section D, Biological crystallography 66, 213–221, doi:10.1107/S0907444909052925 (2010). [PubMed: 20124702]

81. Williams CJ et al. MolProbity: More and better reference data for improved all-atom structure validation. Protein science : a publication of the Protein Society 27, 293–315, doi:10.1002/pro.3330 (2018). [PubMed: 29067766]

82. Pettersen EF et al. UCSF Chimera--a visualization system for exploratory research and analysis. Journal of computational chemistry 25, 1605–1612, doi:10.1002/jcc.20084 (2004). [PubMed: 15264254]

83. Han C et al. Polysome profiling followed by quantitative PCR for identifying potential micropeptide encoding long non-coding RNAs in suspension cell lines. STAR protocols 3, 101037, doi:10.1016/j.xpro.2021.101037 (2022). [PubMed: 34977682]

84. Li B & Dewey CN RSEM: accurate transcript quantification from RNA-Seq data with or without a reference genome. BMC bioinformatics 12, 323, doi:10.1186/1471-2105-12-323 (2011). [PubMed: 21816040]

85. Bray NL, Pimentel H, Melsted P & Pachter L Near-optimal probabilistic RNA-seq quantification. Nature biotechnology 34, 525–527, doi:10.1038/nbt.3519 (2016).

86. Ritchie ME et al. limma powers differential expression analyses for RNA-sequencing and microarray studies. Nucleic acids research 43, e47, doi:10.1093/nar/gkv007 (2015). [PubMed: 25605792]

87. Smyth GK Linear models and empirical bayes methods for assessing differential expression in microarray experiments. Statistical applications in genetics and molecular biology 3, Article3, doi:10.2202/1544-6115.1027 (2004).

88. Jolliffe IT Principal component analysis. 2nd edn, (Springer, 2002).

89. Van Der Walt S, Colbert SC & Varoquaux G The NumPy array: a structure for efficient numerical computation. Computing in science & engineering 13, 22–30 (2011).

90. Reuter JS & Mathews DH RNAstructure: software for RNA secondary structure prediction and analysis. BMC bioinformatics 11, 129, doi:10.1186/1471-2105-11-129 (2010). [PubMed: 20230624]

91. Guo X et al. Mitochondrial stress is relayed to the cytosol by an OMA1-DELE1-HRI pathway. Nature 579, 427–432, doi:10.1038/s41586-020-2078-2 (2020). [PubMed: 32132707]

92. Ochoa D et al. An atlas of human kinase regulation. Molecular systems biology 12, 888, doi:10.15252/msb.20167295 (2016). [PubMed: 27909043]

93. Consortium EP An integrated encyclopedia of DNA elements in the human genome. Nature 489, 57–74, doi:10.1038/nature11247 (2012). [PubMed: 22955616]

94. Davis CA et al. The Encyclopedia of DNA elements (ENCODE): data portal update. Nucleic acids research 46, D794–D801, doi:10.1093/nar/gkx1081 (2018). [PubMed: 29126249]

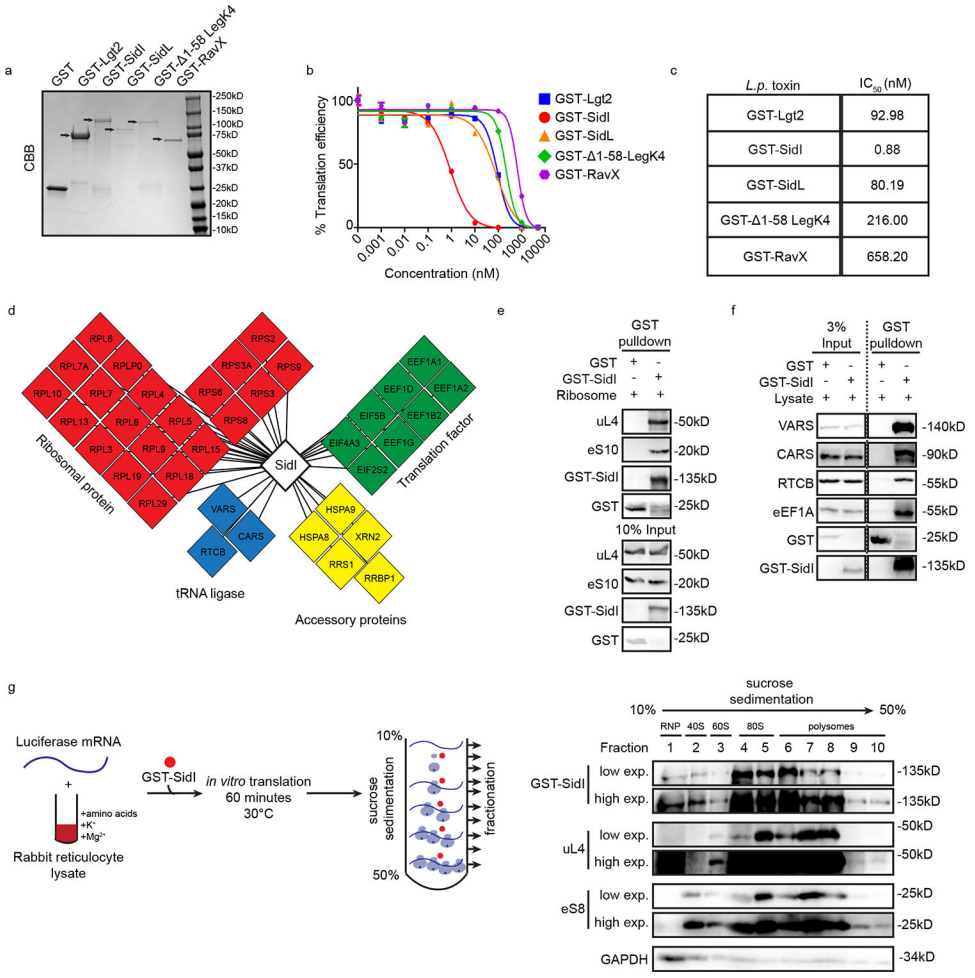

Figure 1. SidI potently inhibits protein synthesis and binds to the cellular translation machinery.

(a) SDS-PAGE and Coomassie brilliant blue (CBB) staining of gels loaded with recombinantly purified GST-tagged *L.p.* EITs (arrows) and GST. (b) Cell free translation of luciferase mRNA in rabbit reticulocyte lysates (RRLs) incubated with purified GST-tagged *L.p.* EITs. Graph depicts the %translation efficiency of luciferase upon incubation with log-fold concentrations of *L.p.* EITs (Data represent mean ± standard error of the mean; n = 3 replicates per treatment condition). (c) IC_{50} values of *L.p.* EITs calculated by non-linear regression analysis. (d) Mass spectrometry analysis of SidI interacting partners from HEK293T and rabbit reticulocyte cell lysates. Cellular translation machinery components enriched by GST-SidI are depicted. (e) GST-SidI pulldown of purified monosomes. Immunoblotting was performed using antibodies against 60S (uL4/RPL4) and 40S (eS10/RPS10) ribosomal proteins and GST. Data are representative of 3 independent experiments. (f) Immunoblot of tRNA interacting proteins VARS (Valine tRNA ligase), CARS (Cysteine tRNA ligase), RTCB (tRNA splicing ligase) and eEF1A precipitated by GST-SidI from HEK293T lysates. Data are representative of 3 independent experiments. (g) Sucrose gradient dependent density centrifugation and fractionation of *in vitro* translation reactions containing luciferase mRNA and GST-SidI. Proteins from each fraction were extracted with

10% TCA, loaded onto SDS-PAGE gels, and immunoblotted with antibodies against GST, uL4 and eS8. Data are representative of 2 independent experiments.

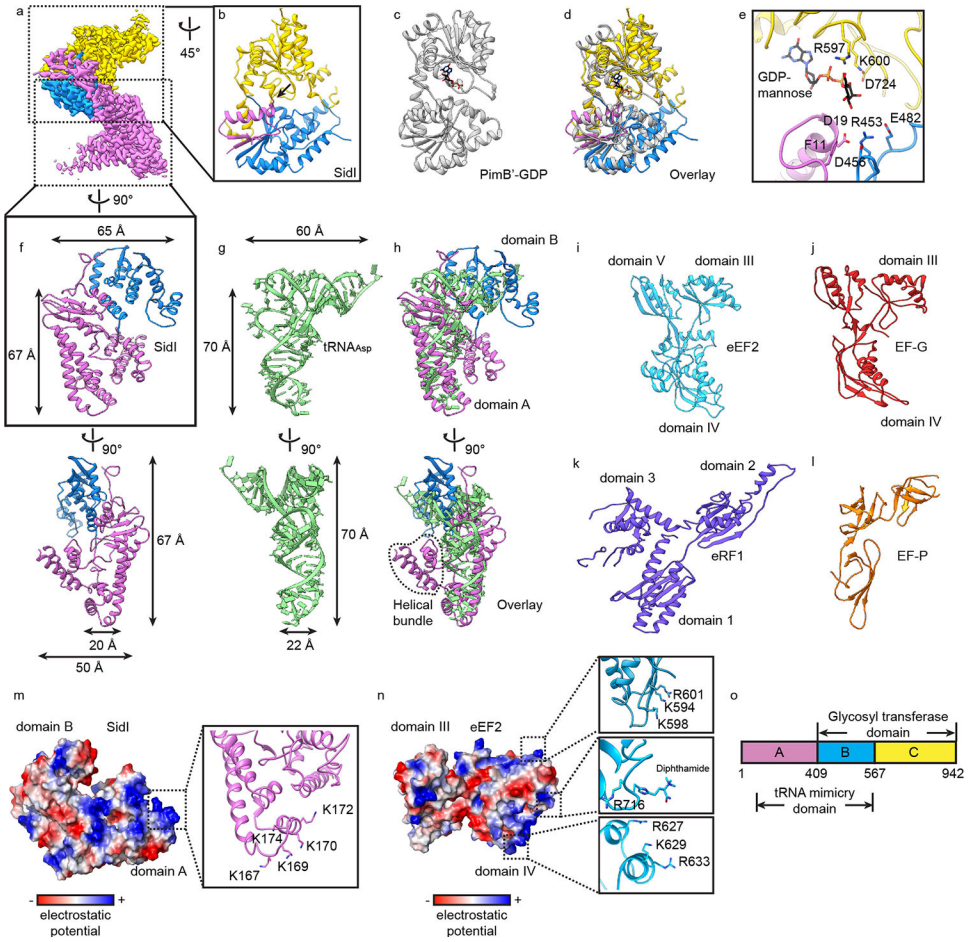

Figure 2. Structural characterization of SidI by cryo-EM reveals tRNA mimicry and glycosyltransferase activity.

(a) Cryo-EM map of SidI with individual domains coloured separately. (b) Rotate view of panel (a) showing the glycosyl transferase domain. Arrow depicts the putative nucleotide-sugar binding cleft. (c) Structure of the mannosyl transferase PimB' from *Corynebacterium glutamicum* bound to GDP in the enzymatic pocket (PDB ID:3OKA). (d) Overlay of (b) and (c) showing the structural similarity between SidI and GDP-PimB'. (e) Enzymatic pocket of SidI with GDP-mannose docked. Amino acids potentially forming direct contact with GDP-mannose or stabilizing the fold of the enzymatic pocket are shown in sticks. (f – h) Structures of the tRNA mimicry domain of SidI in comparison with $tRNA_{Asp}$ with length and width calculated. (i – l) Comparison of the 3D architecture of the tRNA mimicry domains of SidI, eEF2, EF-G, eRF1 and EF-P to the structure of $tRNA_{Asp}$. (m – n) Surface charge distribution of the tRNA mimicry domain of SidI and eEF2 (red - negative charges and blue - positive charges). Box and insets highlight the residues that make up positively charged regions. (o) Schematic representation of the domain architecture of SidI. Domain A of SidI is coloured magenta, domain B in blue and domain C in gold. PimB' is coloured in light grey. $tRNA_{Asp}$ is coloured in green. In all stick representations, atoms are coloured using the CPK scheme.

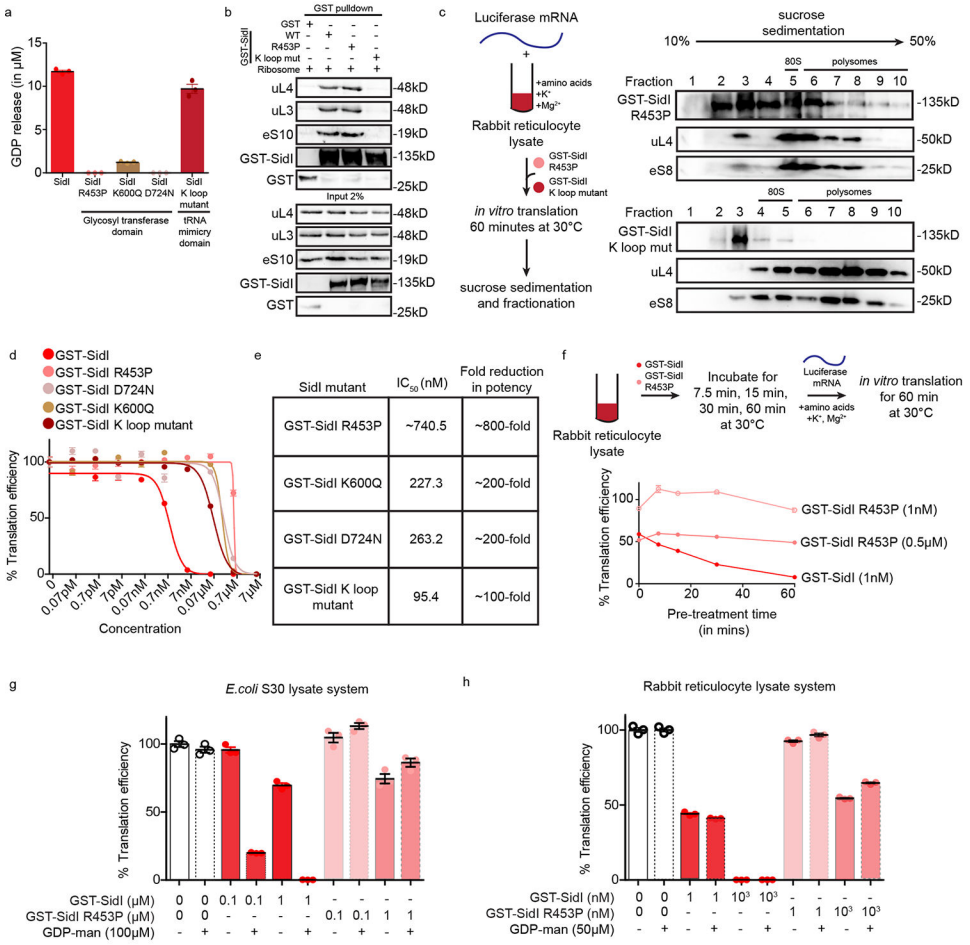

Figure 3. Coupling of tRNA mimicry and enzymatic activity yields SidI potency to target ribosomes and inhibit translation.

(a) GDP hydrolysis assay with GST-SidI wild-type and mutants at 1μM concentration. 50μM of GDP-mannose was provided as a precursor. Graphs depict amount of GDP release in μM (Data represent mean ± standard error of the mean; n = 3 independent replicates per treatment condition). (b) Purified ribosome pulldown with GST, GST-SidI, GST-SidI R453P and GST-SidI K-loop mutant. Immunoblotting was performed using antibodies against uL4, uL3, eS8 and GST. Data are representative of 3 independent experiments. (c) Sucrose gradient dependent density centrifugation and fractionation of *in vitro* translation reactions containing luciferase mRNA and GST-SidI R453P or GST-SidI K-loop mutant. Proteins from each fraction were extracted with 10% TCA, loaded onto SDS-PAGE gels, and immunoblotted with antibodies against GST, uL4 and eS8. Data are representative of 2 independent experiments. (d) Cell free translation of luciferase mRNA in RRLs incubated with purified GST-SidI, GST-SidI R453P, GST-SidI K600Q, GST-SidI D724N or the GST-SidI K-rich loop mutant. Graph depicts the %translation efficiency of luciferase upon incubation with log-fold concentrations of proteins (Data represent mean ± standard error of the mean; n = 3 replicates per treatment condition). (e) IC_{50} values calculated by non-linear regression analysis. (f) Cell free luciferase translation in RRLs pre-treated with GST-SidI or GST-SidI R453P at indicated concentrations. Graph depicts the %translation

efficiency of luciferase with different pre-treatment times normalized to GST control (Data represent mean ± standard error of the mean; n = 3 replicates per time point). (g) Cell free transcription and translation of luciferase mRNA in *E.coli* S30 lysates incubated with GST-SidI or GST-SidI R453P in the absence or presence of 100μM GDP-mannose. Graph depicts the %translation efficiency of luciferase (Data represent mean ± standard error of the mean; n = 3 replicates per treatment condition). (h) Cell free translation of luciferase mRNA in RRLs incubated with purified GST-SidI or GST-SidI R453P in the absence or presence of 50μM GDP-mannose. Graph depicts the % translation efficiency of luciferase (Data represent mean ± standard error of the mean; n = 3 replicates per treatment condition).

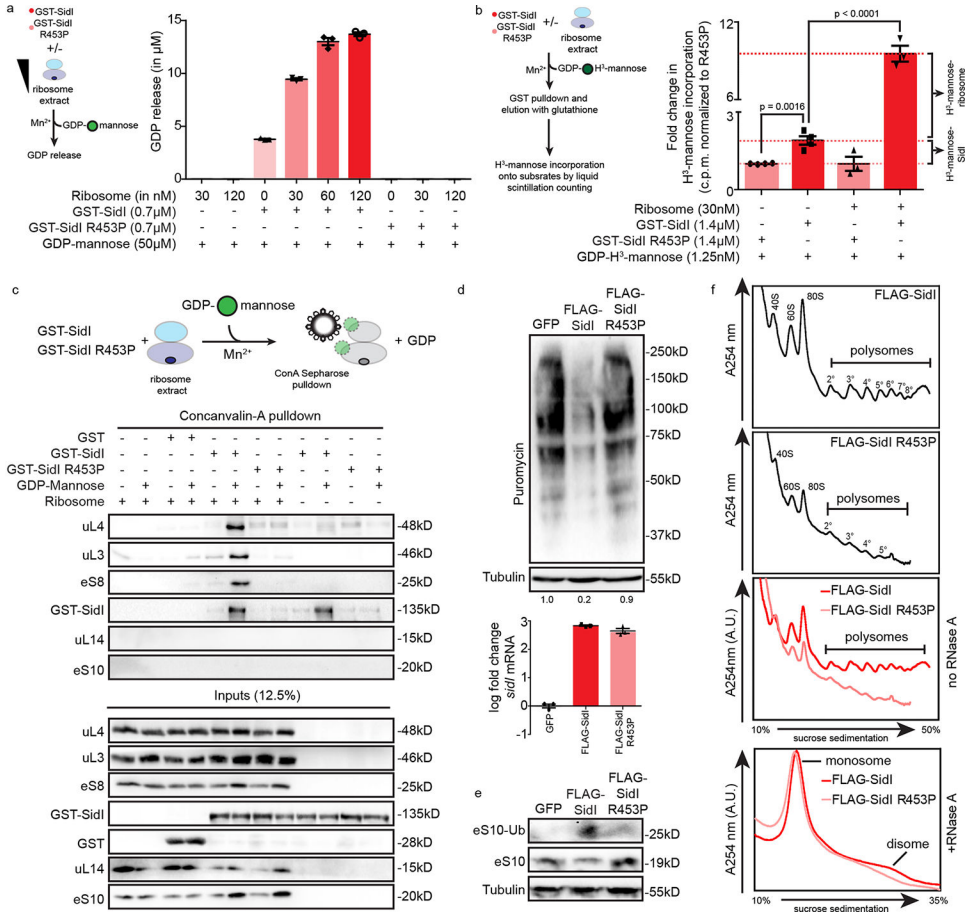

Figure 4. Glycosyltransferase activity of SidI induces ribosome stalling and collisions.

(a) GDP hydrolysis assay with GST-SidI or GST-SidI R453P incubated with increasing amounts of ribosomes purified from HEK293T cells in the presence of 50μM of GDP-mannose as precursor. Graphs depict amount of nucleotide release (Data represent mean ± standard error of the mean; n = 3 replicates per treatment condition). (b) Measurements of H^3-mannose incorporation onto substrates after *in vitro* mannosylation reactions by liquid scintillation counting. 1.25nM radio-labelled GDP-H^3-mannose was used as a nucleotide sugar precursor. Graphs depict fold change in counts per million (c.p.m) normalized to values in reactions containing GST-SidI R453P. Data represent mean ± standard error of the mean from independent experiments - GST-SidI R453P (n = 4); GST-SidI (n = 4); GST-SidI R453P + ribosome (n = 3); GST-SidI + ribosome (n = 3). p-values were calculated by students t-test. (c) Concanavalin-A mediated enrichment of proteins in 30nM ribosome extracts after *in vitro* mannosylation reactions with 1.4μM of GST, GST-SidI or GST-SidI R453P. Immunoblotting was performed using antibodies against uL4, uL3, eS8, uL14, eS10 and GST. Data are representative of 2 independent experiments. Pulldowns and input samples were processed in parallel on separate gels. (d) Cells expressing GFP, FLAG-SidI or FLAG-SidI R453P subjected to puromycin pulse-chase analyses. Immunoblotting of lysates was performed using antibodies against puromycin and Tubulin. Data are representative of 2 independent experiments. Values below the immunoblots in (d) depict densitometric quantification of puromycylated peptides normalized to the amount of Tubulin in cells.

Expression levels of SidI and SidI R453P were determined by qRT-PCR (Data represent mean ± standard error of the mean; n = 3). Data were normalized to the average Ct values of the reference gene ribosomal protein S29. (e) Lysates from cells expressing GFP, FLAG-SidI or FLAG-SidI R453P subjected to immunoblotting using antibodies against eS10. Data are representative of 3 independent experiments. (f) Post nuclear supernatants of cells expressing FLAG-SidI or FLAG-SidI R453P either subjected to ultracentrifugation in 10% - 50% sucrose gradients (no RNase-A) or treated with RNase-A for 15 minutes and subjected to ultracentrifugation in 10% - 35% sucrose gradients (+RNase-A) followed by polysome profiling. For the samples with no RNase treatment, the 40S, 60S and 80S peaks are marked. Progressive polysome peaks mark number of ribosomes per mRNA (2°-disome; 3°-trisome etc.). For the samples treated with RNase, the monosome and disome peaks are marked.

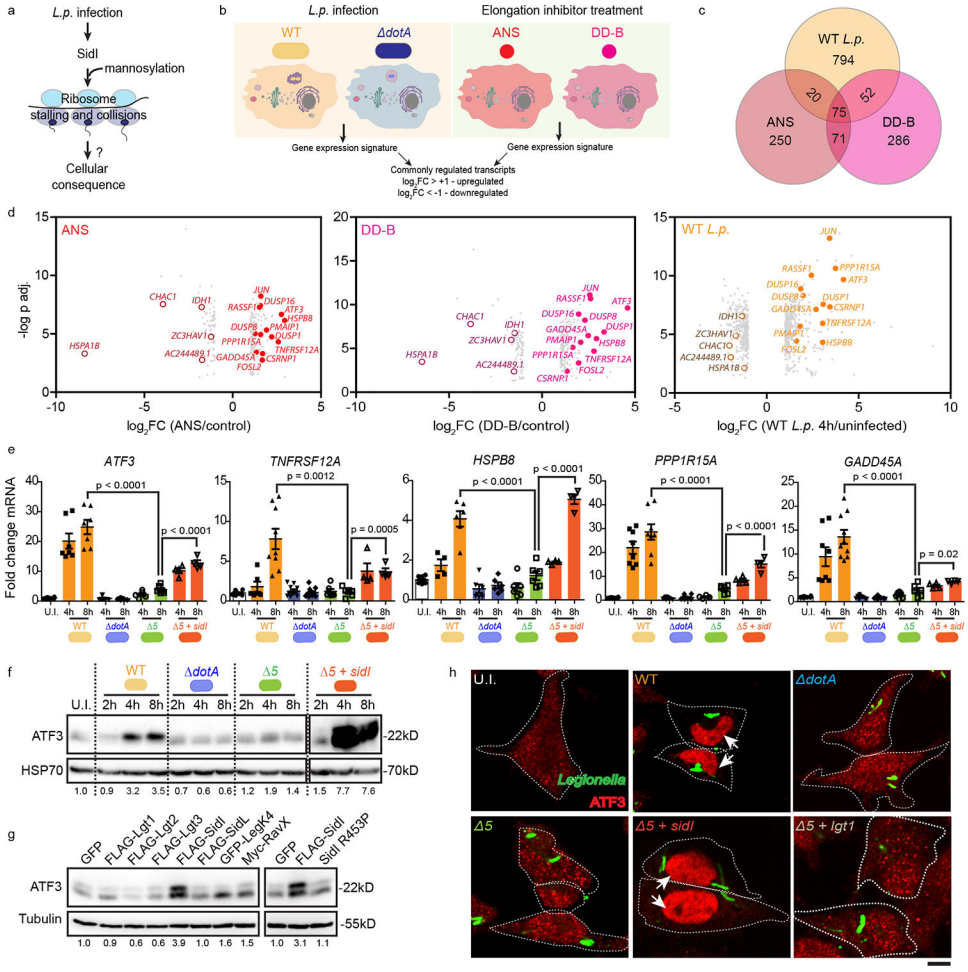

Figure 5. Transcriptional profiling reveals a conserved stress signature activated by SidI-mediated ribosome stress.

(a – b) Schematic model of the RNA-seq pipeline. Expression profiles of HEK293 FcγR cells infected with WT or *ΔdotA L.p.* (MOI = 50) and HEK293T cells treated with anisomycin (ANS, 0.1μM) or didemnin-B (DD-B, 0.1μM) were compared. (c) Venn diagram and (d) $\log_2$fold change induction of differentially expressed co-regulated transcripts between ANS and DD-B treatments for 4 hours in HEK293T cells and WT *L.p.* infection after 4 hours in HEK293 FcγR cells. In (d), values were normalized to respective controls (DMSO for drug treatments and uninfected cells for *L.p.* infections) (n = 2 independent replicates per condition). Upregulated transcripts that map to stress signaling and cell death pathways are highlighted with solid-coloured circles. p-values were calculated using the LIMMA Bioconductor package (5% false discovery rate with an effect size of at least 2x in comparison to controls). LIMMA implements a two-sided moderated t-test with empirical Bayesian shrinkage. (e) Fold change induction of stress inducible transcripts measured by qRT-PCR in HEK293 FcγR cells infected with indicated *L.p* strains (MOI = 50). Data represent mean ± standard error of the mean. n = independent replicates; For *ATF3* panels – U.I. (n = 12), WT 4h (n = 7), WT 8h (n = 7), *ΔdotA* 4h (n = 10), *ΔdotA* 8h (n = 10), *Δ5* 4h (n = 5), *Δ5* 8h (n = 6), *Δ5 + sidI* 4h (n = 4), *Δ5 + sidI* 8h (n = 4); For *TNFRSF12A* panels – U.I. (n = 12), WT 4h (n = 6), WT 8h (n = 9), *ΔdotA* 4h (n = 10), *ΔdotA* 8h (n =

10), *Δ5* 4h (n = 6), *Δ5* 8h (n = 6), *Δ5* + *sidI* 4h (n = 4), *Δ5* + *sidI* 8h (n = 4); For *HSPB8* panels – U.I. (n = 10), WT 4h (n = 4), WT 8h (n = 6), *ΔdotA* 4h (n = 6), *ΔdotA* 8h (n = 6), *Δ5* 4h (n = 6), *Δ5* 8h (n = 6), *Δ5* + *sidI* 4h (n = 4), *Δ5* + *sidI* 8h (n = 4); For *PPP1R15A* panels – U.I. (n = 12), WT 4h (n = 8), WT 8h (n = 8), *ΔdotA* 4h (n = 10), *ΔdotA* 8h (n = 12), *Δ5* 4h (n = 4), *Δ5* 8h (n = 6), *Δ5* + *sidI* 4h (n = 4), *Δ5* + *sidI* 8h (n = 4); For *GADD45A* panels – U.I. (n = 12), WT 4h (n = 8), WT 8h (n = 10), *ΔdotA* 4h (n = 10), *ΔdotA* 8h (n = 10), *Δ5* 4h (n = 6), *Δ5* 8h (n = 6), *Δ5* + *sidI* 4h (n = 4), *Δ5* + *sidI* 8h (n = 4). Expression values were normalized internally to the reference gene *RPS29* and expressed as fold change over the levels in uninfected controls. p-values were calculated by students t-test. (f-g) Immunoblotting of ATF3 in lysates from (f) HEK293 FcγR cells infected with indicated *L.p.* strains (MOI = 50). Data are representative of 3 independent experiments. The samples for infection with *Δ5* + *sidI L.p.* derive from parallel experiments and the blots were processed in parallel; and (g) cells expressing GFP, *L.p.* EITs or FLAG-SidI R453P. Data are representative of 3 independent experiments. (h) Indirect immunofluorescence of ATF3 and *L.p.* in HEK293 FcγR cells infected with indicated *L.p.* strains (MOI = 5) for 6 hours. Scale bar = 10μM. Data are representative of 2 independent experiments. Nuclear region is marked by arrows.

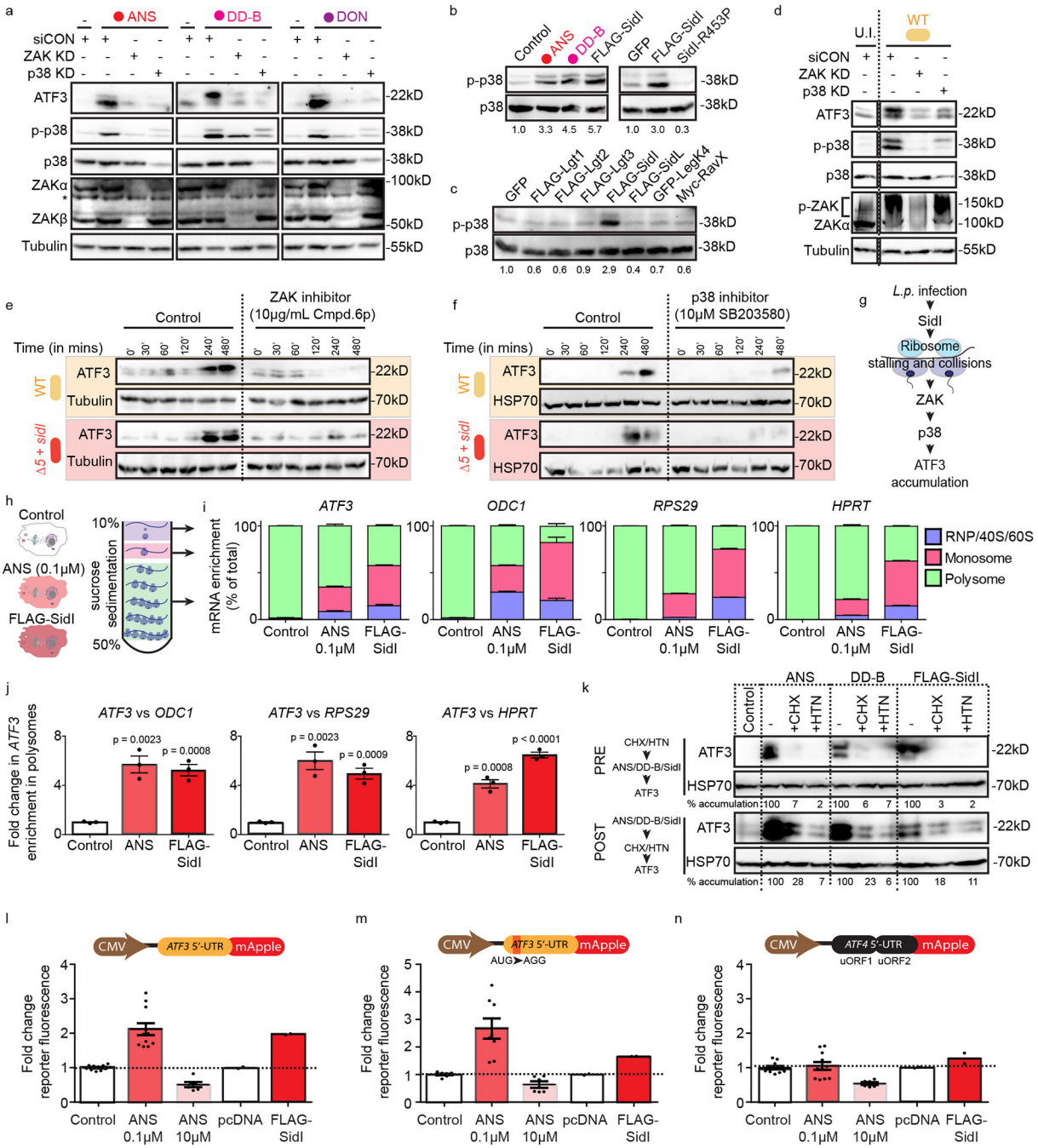

Figure 6. ATF3 accumulation is regulated by kinase signaling and preferential mRNA translation during collided ribosome stress.

(a) Immunoblotting of ATF3, phospho- and total p38, ZAK and Tubulin in HeLa cells depleted for ZAK or p38 by siRNA for 72 hours and treated with ANS (0.1μM), DD-B (0.1μM) or deoxynivalenol (DON, 1μM) for 4 hours. Data are representative of 3 independent experiments. *-unspecific band. (b-c) Immunoblotting of phospho- and total p38 in lysates from HEK293T cells treated with (b) ANS and DD-B for 4 hours or cells expressing GFP, FLAG-SidI, FLAG-SidI R453P or (c) epitope tagged *L.p.* EITs. Values below immunoblots depict densitometric quantification of phospho-p38 band intensities

relative to total p38 and normalized to controls. Data are representative of 2 independent experiments. (d) Immunoblotting of ATF3, phospho-p38, total p38, ZAKα and Tubulin in lysates from HEK293 FcγR cells treated with control siRNA or siRNAs against ZAK and p38 for 72 hours followed by infection with WT *L.p.* (MOI = 50) for 4 hours. Data are representative of 2 independent experiments. Lanes were cropped from the same gel. (e-f) Immunoblotting of ATF3 in lysates from HEK293 FcγR cells infected with WT or *Δ5+sidI L.p.* strains and treated with (e) ZAK inhibitor (Compound 6p, 10μg/mL) or (f) p38 inhibitor (SB203580, 10μM). Data are representative of 2 independent experiments. (g) Schematic of the RSR pathway activated by SidI. (h-j) Targeted ribosome profiling of *ATF3*, *ODC1*, *RPS29* and *HPRT* mRNA in HEK293T cells that are unstressed (control), treated with ANS (0.1μM) or expressing FLAG-SidI (n = 3 independent experiments; data represent mean ± standard error of the mean). Stacked bars in (i) depict % enrichment of mRNA in each collected fraction by qRT-PCR. Graphs in (j) depict fold change in polysome-associated *ATF3* mRNA measured by qRT-PCR. Expression values were normalized internally to polysome-associated *ODC1*, *RPS29 and HPRT* and expressed as fold change over the levels in controls. p-values were calculated by students t-test. (k) Immunoblotting of ATF3 in lysates from HEK293T cells treated with ANS (0.1μM) or DD-B (0.1μM) for 4 hours or cells expressing FLAG-SidI. (PRE) – cells were pre-treated with CHX (50μg/mL) or HTN (10μM) for 1 hour before ANS/DD-B addition or 6 hours after addition of the transfection mix. (POST) – cells were treated with CHX (50μg/mL) or HTN (10μM) 1 hour after ANS/DD-B addition or 24 hours after transfection of FLAG-SidI and lysed after 3 hours. Values below immunoblots depict densitometric quantification of ATF3 band intensities relative to HSP70 and normalized. Data are representative of 2 independent experiments. (l-n) Fold change in median intensities of mApple expression in HEK293T cells transfected with the indicated reporter constructs and treated with ANS or expressing FLAG-SidI relative to controls. For (l) – Control (n = 11); ANS 0.1μM (n = 11); ANS 10μM (n = 6); pcDNA (n = 2); FLAG-SidI (n = 2); For (m) – Control (n = 8); ANS 0.1μM (n = 8); ANS 10μM (n = 6); pcDNA (n = 2); FLAG-SidI (n = 2); For (n) – Control (n = 11); ANS 0.1μM (n = 11); ANS 10μM (n = 6); pcDNA (n = 2); FLAG-SidI (n = 2). For l – n panels, n = independent replicates. Data represent mean ± standard error of the mean for experiments with n>3.

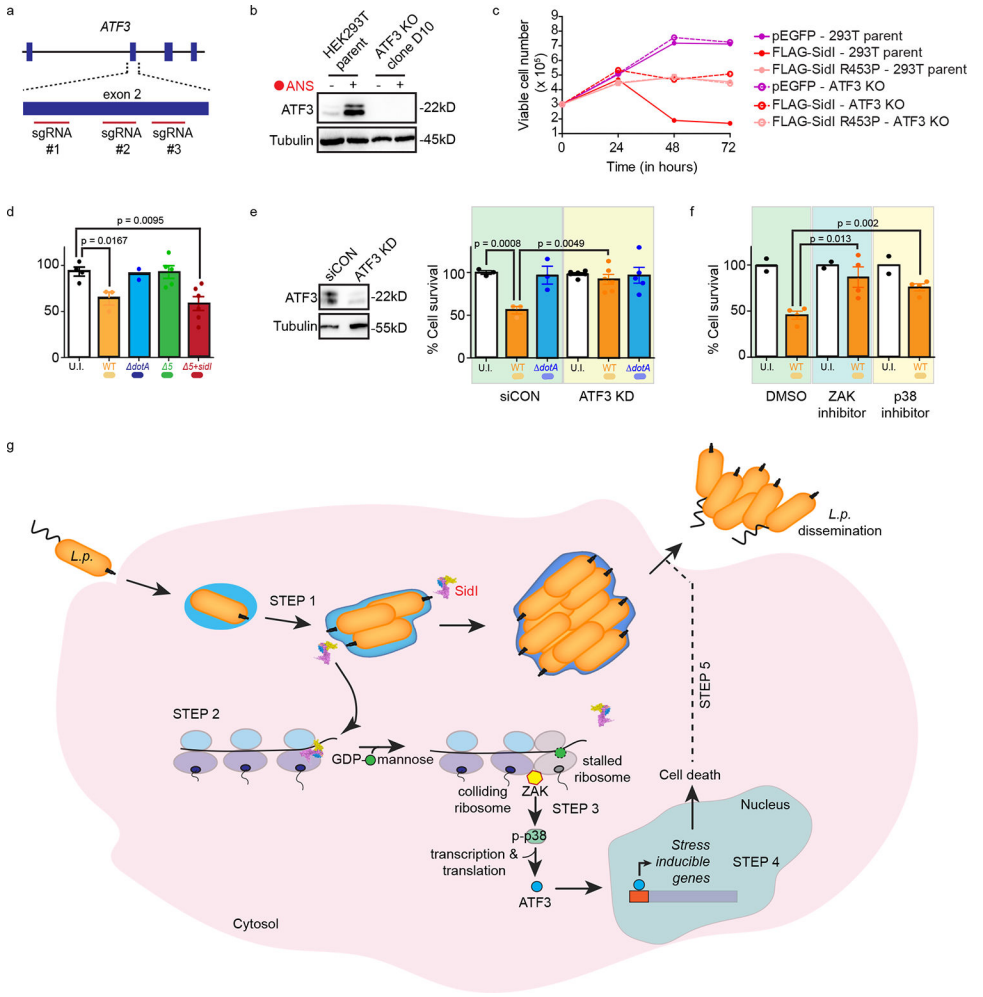

Figure 7. ATF3 orchestrates a transcriptional program that regulates cell fate.

(a) Schematic of the strategy for CRISPR-Cas9 mediated depletion of ATF3 in HEK293T cells. (b) Immunoblotting of ATF3 in lysates from HEK293T parent or ATF3 knockout (ATF3 KO) HEK293T cells at steady state and after challenge with ANS (0.1μM) for 4 hours. (c) Cell viability measurements in parent and ATF3 KO HEK293T cells expressing GFP, FLAG-SidI or FLAG-SidI R453P (n = 2 independent replicates per condition). (d – f) Cell viability measurements in HEK293 FcγR cells (d) infected with WT (n = 3), *ΔdotA* (n = 2), *Δ5* (n = 5) or *Δ5 + sidI* (n = 6) *L.p.* strains, (e) treated with control and ATF3 siRNAs for 72 hours and infected with WT (control: n = 3; siATF3: n = 6) or *ΔdotA* (control: n = 3; siATF3: n = 5) *L.p.* and (f) treated with ZAK inhibitor (Compound 6p, 10μg/mL) or p38 inhibitor (SB203580, 10μM) and infected with WT *L.p.* (n = 4). For d – f panels, n = independent replicates. Data represent mean ± standard error of the mean for conditions with n ≥ 3. All infections were performed at an MOI = 50 for 10 hours. p-values were calculated by students t-test. Immunoblot for ATF3 depicts knockdown efficiency. (g) A five-step schematic model of how *L.p.* hijacks the ribotoxic stress response pathway. Step 1 – *L.p.* infects the host cell, establishes its replicative niche, and secretes SidI into the host cell cytosol. Step 2 – SidI by way of its tRNA mimicry domain is targeted specifically to components of the host translation machinery, including the ribosomes

depicted. In the presence of cytosolic GDP-mannose, SidI mannosylates the ribosome and causes translation elongation defects that result in an accumulation of stalled and collided ribosomes in cells. Step 3 – Collided ribosomes are sensed as ‘aberrant’, resulting in the recruitment and activation of the kinase ZAKα that in turn phosphorylates and activates p38. This stress pathway activation results in the accumulation and translocation of ATF3 from a diffuse cytosolic disposition to the nucleus. Step 4 – ATF3 binds to genomic regions of stress inducible transcripts and regulates their expression. Step 5 – ATF3, via the transcriptional program it orchestrates, induces host cell lysis, thereby potentially resulting in the dissemination of replicated bacteria into the extracellular milieu.